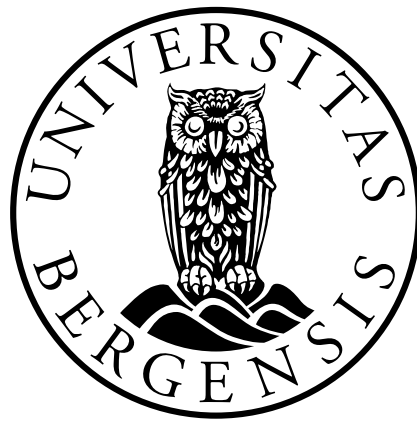# The Shock Structure Problem and Svärd's New Eulerian Model

by

Josef Flatlandsmo

Master of Science Thesis in
Applied and Computational Mathematics

Department of Mathematics
University of Bergen

May 2020

Abstract

The aim of this thesis is to compare the Navier-Stokes equations and a new Eulerian model proposed by [Sva18]. This is done through numerical simulations applied to a shock structure problem. Experimental data from [Ste72] for the density profile of a Mach 8 shock in argon gas is used as a basis for comparison. Different viscosity models (constant dynamic viscosity μ, temperature related power law $\mu \frown T$, Sutherland's viscosity law) are used with different parameters to achieve the closest approximations.

The Eulerian model effectively uses the kinematic viscosity $\nu = \alpha \frac{\mu}{\rho(x,t)} + \beta(\rho, T)$, where ρ is the density. Svärd anticipates that the primary dependency is $\nu \frown \mu(T)$, but the coefficient α is undetermined and reasoned to be either $\alpha = \{1, 4/3\}$. Herein, β is set to zero, and based on the obtained results $\alpha = 4/3$ is suggested to be the more proper coefficient.

The results show that power law viscosity, $\mu \propto T$, produce good approximations for Navier-Stokes equations but the Eulerian model do not manage to capture the shock profile well. However, the Eulerian model capture the shock well, within experimental uncertainties, when constant dynamic viscosity is employed. The closest approximations of both systems are compared and the Eulerian model seem to capture the shock profile slightly better. This might suggest that using a constant dynamic viscosity is more appropriate for the Eulerian model.

Acknowledgements

I especially want to thank my supervisor, Professor Magnus Svärd, for his guidance through this thesis. Fruitful conversations has been growing ground for a steep and fun learning curve and for the right places to retrieve information.

I want to thank my family and friends for support, and particularly my brother who have shown keen interest in this work and functioned as a sparring partner. Discussions with him has enlightened ideas and clarified concepts.

I also want to thank my fellow students for a memorable time and the lecturers I have had, for sharing their knowledge with passion and the encouragement to be curios.

JF, May 2020

Contents

List of Figures

List of Tables

Nomenclature

Notation

$\{\cdot, \cdot, ..., \cdot\}$ Denotes a set.

$' =$ to show that a function is differentiated. For example if $u = u(x)$, then $(F(u(x)))_x = F'(u(x))u'(x)$.

$[\cdot] =$ Vector that contain different quantities. For example for the conserved variables of the Euler equations $[u] = [\rho, \rho\mathbf{v}, E]^T$.

$\frac{d}{dt}(\cdot) = (\cdot)_t$

$\frac{d}{dx}(\cdot) = (\cdot)_x$

$[\cdot, \cdot]$ Denotes a closed interval.

Bold Letters $=$ Vectors. For example the discrete vector $\mathbf{u} = (u_1, u_2, ...u_n)^T$ or the three dimensional velocity vector $\mathbf{u} = (u, v, w)$.

New Eulerian Model $=$ The name of the proposed system by Svard [Sva18] will be denoted by "new Eulerian model/system", "Eulerian model" or simply "Eulerian". Reference to the standard Euler equations will be made explicit where needed.

nodes/grid points: These are used interchangeably.

Abbreviations

CFL Courant-Friedrichs-Lewy condition

D Dimension

K Kelvin

NS Navier-Stokes

ODE Ordinary Differential Equation

PDE   Partial Differential Equation

SAT   Simultaneous Approximation Term

SBP   Summation By Parts

List of Symbols

γ ratio of specific heats

κ thermal conductivity

λ molecular mean free path

μ dynamic viscosity coefficient

μ_v coefficient of bulk viscosity

ϕ viscosity coefficient

$\propto$ proportional

ψ test function with compact support

$\Psi,$ region behind/in front of a shock

ρ density

a boundary accuracy

b variable coefficient

c speed of sound

c_p specific heat capacity at constant pressure

c_v specific heat capacity at constant volume

E energy

e internal energy

h grid size approximating the infinitesimal dx

k_b Boltzmann constant

Kn Knudsen Number

M mach number

m momentum

m_m molecular mass

p pressure

R gas constant

r exponent for viscosity power-law

S stress tensor

s entropy

S_u Sutherland temperature

T temperature

w continuous solution variable

I   electric current

Introduction

The Navier-Stokes equations have been reigning the domain of fluid dynamics for almost 200 years and have been challenged in later times by for example [Bre05]. Recently [Sva18], proposed a new system of equations that he claims are more physically consistent than the Navier-Stokes equations. A main feature of this new system is the introduction of mass diffusion, yielding a set of completely parabolic equations. Conducting numerical experiments on both the new Eulerian system from [Sva18] and the Navier-Stokes system, and comparing these with physical experiments, can give more insight into whether or not the Navier-Stokes should be reconsidered.

A well known, non-equilibrium and simple flow is that of a normal shock wave. Shock waves occur in e.g. in supersonic flight, explosions, detonations, and are disturbances of finite thickness that propagate between supersonic and subsonic fluid. The gradients of the fluid properties are very large in a shock and appear as discontinuities on a macroscopic scale. However, on a microscopic scale a continuous profile is apparent [Kun16]. Therefore, the field variables are simulated on a domain with unit length of upstream molecular mean free path (the inter-molecular mean distance), denoted λ_1.

A normal shock flow gives a good opportunity to numerically capture the shock and has become one standard way of testing hydrodynamic models. Some characteristic features that makes the shock structure problem attractive for numerical simulations are

- It is steady state and one-dimensional

- The upstream and downstream are clearly defined through the Rankine-Hugoniot relations

- Solid boundaries are not present such that boundary effects can be neglected

- All gradients of the field variables vanish far upstream and far downstream

[RD19].

In this thesis a steady state shock at Mach 8 is simulated and compared with experimental data from [Ste72]. The numerical method is based on Summation By Parts Operators with a variable coefficient matrix, making the stencils narrow. These have the inherent ability to dampen the highest frequency mode and extra artificial diffusion is therefore not added. This enables a coarser spatial discretization and relatively fast computations. Due to the fundamental difference in the Navier-Stokes and the Eulerian model of [Sva18], i.e. mass diffusion, different viscosity models are employed and the results compared.

Thesis Outline

Chapter 1 introduce some theory on the conservation laws, the new proposed system by Svärd and some preliminary knowledge concerning shock waves and viscosity.

Chapter 2 is concerned with the numerical disretization. How the different variables are calculated in the code. A procedure for the non-dimensional scaling is shown and how this affects constituting parameters. An explanation of why the the non-dimensional scaling is chosen instead of using the physical parameters from experiment is also explained.

Chapter 3 present the results. First simulations of constant dynamic viscosity is shown, then power laws with different parameters and then results based on Sutherland's viscosity law are presented. Subsequently, the simulations closest to the experimental values are shown and compared for the Navier-Stokes and the new Eulerian model.

Chapter 4 have a discussion regarding the results, points to some weaknesses and reason on uncertainties.

Chapter 5 summarize the results. Some conclusions are drawn and a small list of suggested work for future projects is given.

Chapter 1

Preliminaries

1.1 Shock Waves and the Shock Structure Problem

Defining some terminology for shocks is essential to avoid confusion. All the shocks considered are one-dimensional and stationary in a fixed coordinate system located at x=0. The inflow/upstream side is denoted by "1", and outflow/downstream denoted by "2". The upstream side will be on the left hand side of all figures throughout.

A shock wave is a traveling signal with almost a discontinuous jump in the fluid properties. High gradients of temperature and velocity cause entropy production within in the shock wave. Shocks are very thin, but still of finite thickness, in the order of micrometers [Kun16]. They are often modeled as discontinuities but have continuous change in fluid properties over a characteristic distance of a few mean free paths. This is because the relaxation time for momentum and heat transport is finite [GR07]. This is opposed to acoustic waves which are infinitely thin with regards to change in fluid properties. In the experimental data given by [Ste72], the tube of which the one-dimensional normal shock wave experiments are conducted in, are of large enough diameter, 17inches $\approx$ 432 mm, so that wall friction can be completely neglected. The shock waves studied are steady state shocks. Mathematically one can derive the shock speed, and this is constant given constant upstream and downstream conditions. These constant conditions (Rankine-Hugoniot conditions see Section 1.4) are the basis for the numerical calculations.

For a better understanding of the shock waves and the experimental values, the experimental setup from [Ste72] and the evolution of a normal shock is briefly explained: There is a large reservoir of high pressure gas at the downstream side. This is separated from the shock tube via a diaphragm, which is located next to a "cookie cutter" (sharp blades). In the tube, upstream of the diaphragm there is a low pressure gas resting at zero velocity. When gas pressure of a certain state in the reservoir is achieved, the diaphragm bulges into the cookie cutter and bursts. The high pressure gas enters the tube. Since this gas is at resting velocity in the high pressure chamber, there will be an acceleration of the gas into the tube. This acceleration is a transient phase. The front of the gas builds up speed until it reaches

supersonic speed (w.r.t to upstream) and then further accelerated to reach its shock speed. Now, the shock front is in a steady state, no acceleration (equivalent with no net force according to newtons 2nd law) is apparent, and hence stable profile variables (density, velocity) of the shock front can be measured. Since the downstream gas-reservoir has such a large volume compared to the volume of the tube, the pressure and density do not change significantly during the shock propagation. Therefore, once the shock speed has been reached the shock front propagates with constant speed.

To measure steady state shock density profile, an electron gun and collector (Faraday cage) is used. These are located the equivalent to 55 tube-diameters from the diaphragm position, and measures the electric current flowing through the rarefied gas normal to the gas-flow direction. The cage current is recorded as a function of time. Density as a function of position, is subsequently calculated through an exponential attenuation law and a Galilean velocity transformation, where

$$\rho \propto \log \frac{I}{I_0} \tag{1.1}$$

The thermodynamic behavior of a mono-atomic gas is much simpler than that of poly-atomic gas. It does not possess the modes of rotation or vibration. Also, it does not dissociate and only ionizes at very high temperatures, therefore it is preferred used in shock tube experiments [GR07].

The upstream and downstream conditions are uniquely defined through the Rankine-Hugoniot conditions. There are no solid boundaries to be taken into account.The one dimensional steady state nature of the problem allows for a numerical iteration in time until the solution from two neighboring time steps are less than a small prescribed tolerance.

It is worthwhile to mention that there are other ways of dealing with 1-dimensional flow with shocks. One other standard method is the *Sod Shock Tube Problem*. Here, high- and low pressure gas is partitioned by a diaphragm, located in the middle of the tube/domain, which bursts when the the pressure is high enough. The initial velocity on both sides are zero.

1.2   Continuum hypothesis

At the microscopic spatial scale a fluid consists of discrete molecules, the motions of which are random. They collide with each other and have different velocities. These collisions are part of relaxing any disturbances or non-equilibrium states. This happens on a very small temporal scale [TME12].

The continuum hypothesis is based on the principle that, if the scale one observes the fluid in is large enough, much larger than the mean free path, the discreteness of the fluid vanish and one can define a *continuum* and continuum particles/parcels. That is, a fluid has a continuous variation in all its field variables. Generally in continuum mechanics one assumes that the fluid is in local thermodynamic equilibrium at all instances. This is a result of the temporal scale of the governing equations is much larger than that of the microscopic one.

The well known knudsen number is defined as

$$Kn = \frac{\lambda}{L} \tag{1.2}$$

Where, λ is the mean free path of the molecules and L is a characteristic length scale of the flow. It is used to determine whether a statistical mechanics or continuum mechanics formulation is applicable to model the phenomenon at hand. For $Kn < 0.01$ one considers the fluid as a continuum, for $Kn > 1$ one enters the statistical mechanics regime. Shock waves typically fall between ≈ 0.2 and ≈ 0.3, i.e. an intermediate regime [RD19]. Therefore, when analyzing a shock structure this questions the validity of the local thermodynamic equilibrium assumption and the continuum hypothesis. However, this is in favor for use of the ideal gas law (approximating molecules as small hard spheres with no spatial extent) as an equation of state, as the gas is rarefied.

For a PDE in local formulation, one accepts the continuum hypothesis and the PDE is defined at all (mathematical) points, being infinitely small.

1.3 Conservation Laws and Weak Form Solutions

The conserved quantities for the gas flow herein are mass, momentum and energy. The conservation principles applied to a control volume, and amended by Gauss theorem, Reynolds transport theorem and Fouriers law of heat conduction leads to the equations of conserved variables in local form,

$$\frac{\partial \rho}{\partial t} + \nabla_{\mathbf{x}} \cdot (\rho \mathbf{u}) = 0$$
$$\frac{\partial (\rho \mathbf{u})}{\partial t} + \nabla_{\mathbf{x}} \cdot (\rho \mathbf{u} \otimes \mathbf{u}) + \nabla_{\mathbf{x}} P = div_{\mathbf{x}} S \tag{1.3}$$
$$\frac{\partial E}{\partial t} + div_{\mathbf{x}}(E\mathbf{u} + p\mathbf{u}) = div_{\mathbf{x}} S\mathbf{u} + div_x(\kappa \nabla_{\mathbf{x}} T)$$
$$p = \rho R T, \qquad Ideal\ Gas\ Law$$

where $\mathbf{x} = (x, y, z)$ are Cartesian spatial coordinates, $\mathbf{u} = (u, v, w)^T$ is the velocity vector. ρ, $\rho\mathbf{u}$ and E are the conserved variables: density, momentum and energy. p is pressure; T is temperature; S is the stress tensor for Newtonian fluid; R is the gas constant; μ and κ are the viscosity and thermal diffusivity coefficients, respectively. The set must be closed by an equation of state. The common approximation is the ideal gas law, which also is in accordance with [Sva18] as this work is based on the results and assumptions therein.

This set of equations (1.3) are the Navier-Stokes-Fourier Equations (from here on, referred to as Navier-Stokes for brevity), and they model a perfect, compressible, heat conducting, viscous gas at local thermodynamic equilibrium. Generally the stress tensor contains two different viscosity coefficients stemming from a pure mathematical derivation rooted in tensor analysis. (For an incompressible flow a thermodynamic pressure can not be defined, which implies $\nabla \cdot \mathbf{u} = 0$ and ϕ drops out.) The coefficient of bulk viscosity is

$$\mu_v = \phi + \frac{2}{3}\mu \tag{1.4}$$

and it is known to have an appreciable effect on shock wave structure [Kun16]. However, for simplicity the standard approximation, also known as *Stokes assumption*, is applied herein,

$$\phi + \frac{2}{3}\mu = 0 \tag{1.5}$$

which is found to be accurate in many cases. This simplification may well affect the results of the calculations, and will be addressed briefly in Section 4.4.

The ideal gas law is assumed to be valid and it implies that the internal energy is only dependent on temperature, i.e. $e = e(T)$. A common and good approximation is that the internal energy and temperature are simply proportional [LeV92]

$$e = c_v T \tag{1.6}$$

The total energy is

$$E = \frac{p}{\gamma - 1} + \frac{\rho|\mathbf{u}|^2}{2} \tag{1.7}$$

and the ratio of specific heat capacities

$$\gamma = \frac{c_p}{c_v} \tag{1.8}$$

Stability of a nonlinear problem can be ensured by the energy method, and if the continuous solution is smooth, convergence to the right solution in the discrete sense can be expected [Gus08]. However, when dealing with nonlinear problems with shocks (discontinuities) the solutions are not smooth. Even if the initial conditions are smooth, discontinuities may develop, yielding non-smooth solutions. When facing such problems, a different definition of a what is meant by a solution is required. A second problem is how to deal with these definitions numerically.

The Navier-Stokes equations can be written in a compact form as

$$[u]_t + [F(u)]_x = [G(u, u_x)]_x \tag{1.9}$$

where $[u]_t = [\rho, \rho\mathbf{u}, E]_t^T$, and the remaining terms $[F(u)]_x$ and $[G(u, u_x)]_x$ are readily seen from (1.3). The inviscid limit of Navier-Stokes, that is $[G(u, u_x)]_x \to 0$, are termed the *Euler Equations*. To simplify the following description of shock waves this idea of inviscid limit is considered. Note however, that the idea of characteristics, entropy condition and weak solutions are still valid for the viscous case, since $[u] = [\rho, \rho\mathbf{u}, E]$ are still conserved and the gradients far upstream $(x \to -\infty)$ and downstream $(x \to +\infty)$ vanish.

As an example, applying the method of characteristics on a *scalar* conservation law of the form

$$\begin{cases} u_t + F(u)_x = 0, & \in \mathbb{R} \times (0, \infty) \\ u = g, & on \quad \mathbb{R} \times (t = 0) \end{cases} \tag{1.10}$$

shows that in general some characteristics intersect. That is, there is not a unique solution. Shock waves introduce discontinuities and therefore dot not satisfy the PDEs in the classical sense. The need to define a solution a different way is apparent. Multiplying (1.10) with a test function with compact support

$$\psi : \mathbb{R} \times [0, \infty) \rightarrow \mathbb{R}, \quad \textit{is smooth with compact support} \qquad (1.11)$$

such that

$$0 = \int_0^\infty \int_{-\infty}^\infty (u_t + F(u)_x)\psi \, dx dt \qquad (1.12)$$

Integration by parts and using the initial condition, the following identity is obtained

$$\int_0^\infty \int_{-\infty}^\infty u\psi_t + F(u)\psi_x \, dx dt + \int_{-\infty}^\infty g\psi \, dx = 0 \qquad (1.13)$$

where $u = u(x, t)$ and $\psi = \psi(x, t)$.

Weak forms of the equations are valid even across the discontinuities as can be seen from (1.13), as it does not depend on the derivatives of the variables in the original form [Eva10]. Note that most of the boundary terms that normally arise from the integration, vanish here due to compact support of ψ. Suppose that (1.10) do have an integral solution, and suppose that u is smooth and uniformly continuous on both sides of the discontinuity. Then by choosing two test functions ψ (one for each region) with compact support, integration by parts yield for each region

$$0 = \int_0^\infty \int_{-\infty}^\infty u\psi_t + F(u)\psi_x \, dx dt = -\int_0^\infty \int_{-\infty}^\infty (u_t + F(u)_x)\psi \, dx dt \qquad (1.14)$$

Since the final integrand has to be zero, the conservation law in each region is satisfied separately

$$u_t + F(u)_x = 0, \quad \textit{in } \Psi_L \qquad (1.15)$$

$$u_t + F(u)_x = 0, \quad \textit{in } \Psi_R \qquad (1.16)$$

where Ψ_L and Ψ_R denote the left and right region separated by the discontinuity, respectively.

Defining a smooth curve separating the two regions, and then defining a normal vector at the curve pointing out of the region Ψ_L and into Ψ_R, one can further show, using (1.15), (1.16) and (1.13), that

$$F(u_L) - F(u_R) = \sigma(u_L - u_R) \qquad (1.17)$$

where σ is the shock speed. Again, see [Eva10] for the omitted details. This is called the *Jump Condition* or the *Rankine-Hugoniot Condition* along the shock curve. The final point is that, even though all the quantities in (1.17) may change, they must always exactly balance.

Weak forms are known to have more than one solution. To choose the physically consistent solutions the entropy condition is introduced, see [Eva10] for details. Physically, this arises from the second law of thermodynamics and the outcome is an entropy production across the shock. The entropy condition for a scalar conservation law is

$$F'(u_L) > \sigma > F'(u_R) \tag{1.18}$$

for a shock wave moving from left to right. This shows that the upstream/left variables are transported faster than the downstream/right.

Entropy production within a shock is caused by heat conducting and viscous processes. As is seen from equation (1.25) the entropy increase is solely determined by the upstream mach number. The magnitude of μ and κ, only determine the thickness of the shock, or said another way, the spatial extent in which the dissipation takes place [Kun16].

A general vector form of the conservation law, such as the Euler equations, with the shock speed σ can be written as,

$$[u_t] + [F(u)]_x = 0 \tag{1.19}$$

where F has a nonlinear vector dependency on u. Now, Rankine-Hugonuiot jump condition for this set of equations gives the general form,

$$[F(u_L)] - [F(u_R)] = \sigma([u_L] - [u_R]) \tag{1.20}$$

and it is immediately understandable that the set of equations are linearly dependent (owing to the vector form), hence the states upstream and downstream of a shock are not arbitrary [Gus08].

1.4   Rankine-Hugoniot Relations

I light of the previous section (Section 1.3), the Rankine-Hugoniot relations are now presented. They give the relation between upstream and downstream conditions across a shock. See for example [Kun16] for a derivation.

The jump condition together with a moving co-ordinate system (moving with the shock) yields the Rankine-Hugoniot conditions,

$$\frac{p_2}{p_1} = \frac{2\gamma M_1^2 - (\gamma - 1)}{\gamma + 1} \tag{1.21}$$

$$\frac{\rho_2}{\rho_1} = \frac{v_1}{v_2} = \frac{(\gamma + 1)M_1^2}{(\gamma - 1)M_1^2 + 2} \tag{1.22}$$

$$M_2^2 = \frac{(\gamma - 1)M_1^2 + 2}{2\gamma M_1^2 + 1 - \gamma} \tag{1.23}$$

$$\frac{T_2}{T_1} = 1 + \frac{2(\gamma - 1)}{(\gamma + 1)^2} \frac{\gamma M_1^2 + 1}{M_1^2}(M_1^2 - 1) \tag{1.24}$$

$$\frac{s_2 - s_1}{c_v} = ln\left(\left[1 + \frac{2\gamma}{\gamma + 1}(M_1^2 - 1)\right]\left[\frac{(\gamma - 1)M_1^2 + 2}{(\gamma + 1)M_1^2}\right]^\gamma\right) \qquad (1.25)$$

where, 1 and 2 as subscripts denote upstream and downstream, respectively.

One solution to (1.23) is $M_1 = M_2$. However, on further analysis this violate the second law of thermodynamics. Therefore, by the entropy condition (1.18), $M_1 = M_2$ is discarded as a solution. Physically this means that shock waves cannot occur unless $M_1 > 1$, which in turn means that $M_2 < 1$, with consequent increase in pressure, density and temperature behind the shock [Kun16].

1.5   Steady State Shock

There are two different ways of dealing with steady state shocks. One way is to look at the steady equations, i.e.,

$$\frac{\partial(\cdot)}{\partial t} = 0 \implies [F(u)]_x = [G(u, u_x)]_x \qquad (1.26)$$

See for example [RD19], [GR07] or [ESM05].

In this thesis, the time dependencies are kept, and the computations are done in a coordinate system moving with the shock. Hence, the equations are of the form

$$[u]_t + [F(u)]_x = [G(u, u_x)]_x \qquad (1.27)$$

1.6   New Eulerian Model

The inconsistencies of the Navier-Stokes equations, argued for in [Sva18], lead to a different set of equations that model fluid flow in general terms. In short, the important points from [Sva18] regarding these inconsistencies are

- **Positivity**: A physical constraint on a fluid model is positive temperature and density. Artificial diffusion is often needed in numerical codes to avoid negative values. Adding mass diffusion resolves this.

- **Adiabatic Wall**: Navier-Stokes allows for $E_x \neq 0$ and $s_x \neq 0$ at an adiabatic wall, since in general $\rho_x \neq 0$. The claim is that this is an unphysical modelling. If mass diffusion is included in the model then one more boundary condition is needed, $\frac{\partial \rho}{\partial n} = 0$ (normal derivative), which resolves the this issue.

- **Far Field Boundary Conditions**: Linear analysis of far field boundary conditions shows that for any flow with subsonic outflow the Navier-Stokes is incompatible with the Euler equations. That is, the Euler equations are not the inviscid limit of the Navier-Stokes equations. If mass diffusion is included, the system would become completely parabolic and the inconsistency resolved.

- **Entropy at Supersonic Outflow**: A bound on the global entropy, $-\rho s$, is impossible to obtain since the boundary term is indefinite. Alternative entropy functions circumvents this for the Euler equations but such functions do not exist for the Navier-Stokes equations. Again, mass diffusion is the remedy.

- **Relaxation to Thermodynamic Equilibrium**: Due to the continuum hypothesis, the natural dominating process on a *sub-continuum* scale is diffusion. Svärd shows through an example, that a small disturbance in ρ and T, for a fluid at rest ($u = 0$), with no pressure gradient ($p_x = 0$), induces a velocity whose function is to redistribute mass to achieve local thermodynamic equilibrium. This shows that diffusion is *not* the natural dominating process on the sub-continuum scale. However, Navier-Stokes is based on this assumption. Yet another contradicting matter.

- **Frame of Reference**: Using a Lagrangian frame of reference, the fluid parcels are modeled as having constant mass, that is, mass diffusion is non-existent. In an Eulerian frame of reference, the stresses in Navier-Stokes are caused by diffusion which in turn implies *not* constant mass. Heat however, *is* modeled as diffusive in an Eulerian frame with control volume argument, which implies that energy transfer must occur via molecular collisions exactly on the boundary (with no molecular transport across) in between control volumes.

The resulting set of equations, termed Eulerian model, that model a perfect, compressible, heat conducting, viscous gas at local thermodynamic equilibrium is

$$\frac{\partial \rho}{\partial t} + div_{\mathbf{x}}(\rho \mathbf{v}) = \nabla_{\mathbf{x}} \cdot (\nu \nabla_{\mathbf{x}} \rho)$$

$$\frac{\partial(\rho \mathbf{v})}{\partial t} + \nabla_{\mathbf{x}} \cdot (\rho \mathbf{v} \otimes \mathbf{v}) + \nabla_{\mathbf{x}} p = \nabla_{\mathbf{x}} \cdot (\nu \nabla_{\mathbf{x}} \rho \mathbf{v})$$

$$\frac{\partial E}{\partial t} + div_{\mathbf{x}}(E\mathbf{v} + p\mathbf{v}) = \nabla_{\mathbf{x}} \cdot (\nu \nabla_{\mathbf{x}} E)$$

$$p = \rho R T, \qquad Ideal\ Gas\ Law$$

(1.28)

From the new model a different viscosity is proposed to be consistent, namely a kinematic viscosity denoted by ν. It has the following form

$$\nu = \alpha \frac{\mu(T)}{\rho(x,t)} + \beta(\rho, T) \tag{1.29}$$

where $\alpha \in \{1, 4/3\}$, but other values of α may be more appropriate if tested against experiments. The main dependency however is anticipated as $\nu \backsim \frac{\mu(T)}{\rho}$. In accordance with [Sva18] $\beta(\rho, T) = 0$ in this work.

1.7 Viscosity and Gas Properties

The effect of viscosity, μ, on the shock profile is significant, and an accurate model is hard, if not impossible to obtain. Viscosity is the main concern of much research. Therefore, an appreciable amount of the deviation between the numerical calculations herein and the experimental results for comparison, can be attributed to this. However, the main focus of this thesis is to compare the Navier Stokes equations with the new Eulerian model of [Sva18], and see how well they approximate the real physical values. As long as the two systems are based on the same grounds it is hopefully possible to distinguish the effects of viscosity from the fundamental

differences in the two. The following regarding viscosity is based on [GR07] which does an elaborate reasoning of how to model viscosity. They include shock tube experiments from [Als76], [Ste72] and [Sch69], to fit their viscosity model. The main lines are the following assumptions:

- $\mu \propto T^r$

- The assumption of an inverse power law of temperature for inter-molecular forces is made. This introduces a coefficient ζ in the exponent.

- r and ζ are related via the following relation

$$r = \frac{1}{2} + \frac{2}{\zeta - 1} \tag{1.30}$$

The result is the well known power law relation

$$\mu = AT^r \tag{1.31}$$

Where, theoretically $0.5 < r < 1$, but for most real gases $0.64 < r < 0.84$. The r parameter is determined by fitting the values to experimental values of dynamic viscosity, μ, as a function of temperature, T. The values of r they present, are

- r = 0.68, their best fit for Mach Numbers up to 4.4

- r = 0.76, their best fit for Mach up to 12.5

- r = 0.72, the mean of the best fit values. This value is also used by [Als76] to fit values of Direct Monte Carlo Simulations to his shock tube experiments.

They set $A = 1$, since they scale the equations in a non-dimensional form, using $\mu_1 = 1$ and $T_1 = 1$, A becomes independent of r. Please see [GR07] for further justification of this.

Another suggested power law, employed in [RD19], is also used as a viscosity model herein. This has a similar form as the above except that A is substituted with γ^r such that

$$\mu = \gamma^r T^r \tag{1.32}$$

Sutherland's viscosity law is a well known. It has much of the same characteristics as the powerlaws, and in the limit $S_u = 0$ it gives the same powerlaw relation as for hard spheres ($r = 0.5$). It has the form

$$\mu = \mu_{ref} C_1 \frac{T^{3/2}}{T + S_u} \tag{1.33}$$

where,

$$C_1 = \frac{\mu_{ref}}{(T_{ref})^{3/2}}(T_{ref} + S_u) \tag{1.34}$$

u_{ref}, T_{ref} are reference values to be chosen, and S_u is the Sutherland temperature [Sut93].

The common way of relating thermal conductivity, κ, and dynamic viscosity, μ, is through the Prandtl number

$$Pr = \frac{c_p \mu}{\kappa} \tag{1.35}$$

This is a theoretical derived relationship from kinetic theory by [HCB55].

For a mono-atomic gas $Pr = 2/3$. This relationship is based on the premise that the molecules are hard spheres. In the numerical simulations herein, power laws of viscosity (and constant viscosity) is used. The underlying assumption for these is that the inter-molecular force is inverse proportional to radial distance, that is, molecules *not* being hard spheres. Therefore an error of logic/inconsistency. However, the difference in the Prandtl number is small if it follows the power law, and the resulting outcome is not of noteworthy effect (test simulations have been made herein, by changing the Prandtl number), therefore the $Pr = 2/3$ is used throughout.

For a mono-atomic gas, the ratio of specific heats is given by kinetic theory

$$\gamma = \frac{5}{3} \tag{1.36}$$

Since the gas is considered ideal, the following relations of sound and gas constants hold

$$c = \sqrt{\gamma R T} = \sqrt{\gamma \frac{P}{\rho}} \tag{1.37}$$

$$R = c_p - c_v = \frac{k_b}{m_m} = \frac{c^2}{\gamma T} \tag{1.38}$$

where, k_b, is the Boltzmann constant and m_m the molecular mass [LeV92].

1.8 Summation By Parts Operators

Usually when solving non-linear convective problems, such as (1.3), with central differences, artificial dissipation has to be employed to dampen the unresolved highest frequency mode [Mat03]. A common problem and reason for failure for numerical codes is the resulting negative values of density, when clearly this is a strictly positive quantity. As an example of how artificial dissipation works, consider mass conservation of (1.3) equation with artificial dissipation added at the right hand side

$$\rho_t + (\rho u)_x = Ch\rho_{xx} \tag{1.39}$$

for some scaling constant, $C \propto u$, and h being a measure of the grid size. It is readily seen that $h \to 0 \implies Ch\rho \to 0$, such that the equation approaches the true mass conservative equation for finer grid sizes [Sva18]. Artificial dissipation decreases the accuracy and therefore undesirable to use, however there are many ways to do this. See for example [MSN04] for a stable and accurate artificial dissipation in the SBP environment .

In these simulations *compatible narrow stencil SBP operators* are used. These dampen the highest frequency mode without the addition of extra dissipation terms, as opposed to *wide* stencils, making the narrow stencils potentially more accurate than wide stencils [MSS08]. The compatibility is proven by [MSS08] to be a necessary condition for proving stability (i.e. satisfy energy estimate) when combinations of mixed and non-mixed second derivatives are present. No extra dissipation was needed to achieve stable simulations herein.

Summation by parts is the discrete version of integration by parts and paves the way for energy estimates. One popular and effective method for incorporating boundary conditions is the SAT (Simultaneous Approximation Term). However, stability is not shown herein, and it is more difficult to show stability for narrow SBP stencils than wide [MSS08]. Due to the nature of the problem with fixed boundary conditions, the SAT boundary procedure is not needed for stable calculations, and the simplistic injection method is employed instead. In general, the injection method destroys the SBP property which makes the energy estimates/boundedness impossible to obtain [Mat03]. See for example [NC99] or [SCN07] for stability regarding the Navier-Stokes equations using the SAT method in 1D, and in 3D with far field boundaries, respectively.

Chapter 2

Numerical Discretization

2.1 Spatial Discretization

For more details regarding the following SBP setup, the reader is referred to [Mat12]. The simulations were done on a domain $[-12, 12]$ in units of mean free paths to comfortably fit the shock. Note that the length of the domain do not alter the shock structure as long as it is wide enough. For lower Mach numbers, one would need wider simulation domains as the shocks are thicker. The domain, was discretized into N equidistant nodes.

$$x_i = ih, \quad i = 0, 1, 2, ..., N, \quad h = \frac{1}{N} \tag{2.1a}$$

Let w be the continuous solution variable representing ρ, u or E. Define a *discrete* solution vector $\mathbf{v} = [v_0, v_1, ..., v_N]^T$, such that, $v_i = w(x_i)$. Then, at every node x_i, there is associated an unique value v_i.

The first derivative is approximated by the standard central differential operator D_0, the second derivative approximated by D_2. The second derivative with variable coefficient is approximated by the special operator $D_2^{(b)}$, where b is the variable coefficient. This yield a more accurate representation than the straight forward implementation of the first derivative twice, $D_o(b(x)D_o)(\cdot)$. The explicit form of these operators can be found in Appendix A.

The variable coefficient matrix approximates the term $\frac{d}{dx}(b(x)\frac{d}{dx})(\cdot)$. In the Navier-Stokes momentum equation $b = \frac{4}{3}\mu$. In the energy equation there are two instances: $b = \frac{4}{3}\mu u$ and $b = \kappa$. In the Eulerian model $b = \nu$. The semi-discrete form of the Navier-Stokes equations (1.3) in 1D using Stokes assumption (1.5) is,

$$(\rho_i)_t + D_0 m_i = 0$$
$$(m_i)_t + D_0(u_i m_i + p_i) = D_2^{(\frac{4}{3}\mu_i)} u_i \tag{2.2}$$
$$(E_i)_t + D_0(u_i(E_i + p_i)) = D_2^{(\frac{4}{3}\mu_i u_i)} u_i + D_2^{(\kappa_i)} T_i$$

The semi-discrete form of New Eulerian model (1.28) in 1D

$$(\rho_i)_t + D_0 m_i = D_2^{(\nu_i)}\rho$$
$$(m_i)_t + D_0(u_i m_i + p_i) = D_2^{(\nu_i)} m_i \qquad (2.3)$$
$$(E_i)_t + D_0(u_i(E_i + p_i)) = D_2^{(\nu_i)} E_i$$

Where, $\nu_i = \alpha \frac{\mu_i}{\rho_i}$. These discretizations is 2nd order accurate in the interior and 1st order on the boundary.

The simulations were done on a grid of $N = 200$ nodes. However, with Section 1.8 in mind and the decrease in accuracy due to artificial dissipation, 100 and 800 nodes simulations were also done and compared. Though, very time consuming, 800 nodes were not used for all the cases but enough to be certain that 200 nodes gave the same results. Therefore, the 200 nodes simulations are shown.

Note that, when using upwind or downwind schemes, it requires one to distinguish between direction of signal/flux propagation. This is often done using a non-conservative form of the equations and defining a jacobien-matrix with *characteristics* stemming from the differentiation of the flux terms. The scheme used here however, is a central difference scheme written in conservative form and the above mentioned considerations are not needed. See for example [Che11] for a comparison of Navier-Stokes and the Bhatnagar–Gross–Krook equations on the shock structure problem with an upwind method.

2.2 Time Discretization

Commonly, a procedure to numerically solve time- and spatial-dependent PDEs, is to first use a semi-discrete scheme for the spatial discretization to obtain a system of time-dependent ODEs. Then this is discretized by an ODE solver. Stability is of great concern and for smooth solutions, linear stability analysis in many cases suffice. However, for solutions with discontinuities, a stronger measure of stability is often required [GST01]. Convection-diffusion-equations discretized by finite central differences of second-, fourth- and sixth-order, are proved to give strongly stable Runge-Kutta schemes in [LT98].

The classical fourth-order and four-stage Runge-Kutta scheme is used for time marching herein and is given below. Note that the system of equations studied here do not have explicit time dependencies and therefore the Runge-Kutta scheme simplifies,

$$\tilde{u}^{k+1} = \tilde{u}^k + \frac{1}{6}[K_1 + 2K_2 + 2K_3 + K_4] \qquad (2.4)$$

where

$$\begin{cases} K_1 = \mathbf{F}(\tilde{u}^k) \\ K_2 = \mathbf{F}(\tilde{u}^k + \frac{\Delta t}{2}K_1) \\ K_3 = \mathbf{F}(\tilde{u}^k + \frac{\Delta t}{2}K_2) \\ K_4 = \mathbf{F}(\tilde{u}^k + K_3) \end{cases} \qquad (2.5)$$

2.2.1 Time stepping and CFL condition

The Courant-Friedrichs-Lewy (CFL number) condition, gives a limit to how large the time steps, Δt, can be in an explicit time-stepping scheme, such as the Runge-Kutta method. The rationale of the condition is that, the signal with the highest velocity, can not cover more than one cell (node to neighboring node) at each time step. In the case of the shock structure problem

$$\Delta t_{max} = \frac{\Delta x}{max(|u_{max}| + c_{max})} \tag{2.6}$$

In this work the most convenient size of Δt was found through trial and error with the CFL condition as a starting point. One interesting artifact, yet of noticeable concern, is that the Eulerian model (2.3) allowed for (stable simulations) time steps more than 6 times as large than for (2.2), when using classical fourth-order Runge-Kutta. However, the time steps were kept the same for both systems due to the same L_2-norm criterion.

2.3 Solution Procedure

2.3.1 Numerical Code

All scripts and programs were coded from scratch in MATLAB. One main script was used for both models. The only differing part was an extra subroutine to calculate $\nu = \alpha\frac{\mu}{\rho}$ for the Eulerian model. Otherwise, only inputs to the variable coefficient matrix, $D_2^{(b)}$, differed for the two systems. This ensured that there were no differences due to coding and bugs. For each time step at node i, pressure, velocity, temperature, speed of sound and Mach number was computed as

$$\begin{aligned}
p_i &= (\gamma - 1)(E_i - \frac{1}{2}\frac{m_i^2}{r_i}) \\
u_i &= \frac{m_i}{r_i} \\
T_i &= \frac{p_i}{r_i R} \\
c_i &= \sqrt{\gamma\frac{p_i}{r_i}} \\
M_i &= \frac{u_i}{c_i}
\end{aligned} \tag{2.7}$$

In the case of power-law model for the viscosity, μ was computed as

$$\mu_i = AT_i^r, \quad A = \{1, \gamma^r\} \tag{2.8}$$

at node i. Then, the variable coefficient b_i, was computed as seen in (2.2) and (2.3).

Likewise for Sutherland's viscosity law

$$\mu_i = \mu_{ref} C_1 \frac{T_i^{3/2}}{T_i + S_u} \tag{2.9}$$

where $\mu_{ref} = 1$.

2.3.2 Experimental Data

The experimental density data for comparison in this thesis are from [Ste72]. This is the only known source with raw data (given as data points ρ vs. x/λ. The other experimental articles mentioned here, only present the graphs). However, the lack of information therein regarding physical parameters and the scaling used to present the data, other sources must be looked into. Alsmeyer [Als76], do include the data from [Ste72] and compare with his own findings. The work of [Sch69] preceded the work of [Ste72] and the same experimental procedure is used.

The experimental density data in [Ste72] and [Als76] is given in normalized form

$$\rho^* = \frac{\rho - \rho_1}{\rho_2 - \rho_1} \tag{2.10}$$

where ρ is the experimental determined value, ρ_1 and ρ_2 are the upstream and downstream boundary densities, respectively. In the literature of [Ste72], [Als76] and [Sch69], *only* the upstream values of pressure and Mach number are given. However, the temperature *or* density, are not explicitly mentioned anywhere which are needed to fully describe the system. Neither is the value of μ_1 or c_1 stated explicitly.

In [Als76] there is a *footnote* (on page three, section three) stating the value of the mean free path of argon gas at T=300K and p_1=50mTorr. However, it *does not* say that the experiments in fact are conducted at these thermodynamic states. This introduces uncertainties in how to use the experimental data.

Greenshields and Reese [GR07], and Reddy and Dadzie [RD19] acknowledge this, and non-dimensionalize every quantity. On the other hand, [ESM05] takes for granted that the temperature of the experiments in [Als76] is conducted at $T_1 = 300K$.

The interpretation chosen, herein, of the footnote is that: Since there is no characteristic scale to compare with in these shock experiments, a scaling that works well for the x-axis for most Mach numbers, is the relation $\frac{x}{\lambda_1}$ where, $\lambda_1 = \frac{16}{5\sqrt{2\pi\gamma}}\frac{c_1\mu_1}{p_1}$ is the mean free path for argon gas at said upstream thermodynamic values ($T_1 = 300K$, $p_1 = 50$mTorr, μ_1 and c_1 are retrieved from tables). This scaling of the x-axis ensures that the resolution of the shock is small enough and the shock features are well presented in the graphs. Choosing a large λ_1, one would need a very large domain, and choosing a small λ_1, the resolution is to coarse and the shock appear as a jump (unless one uses a very small domain, i.e. fractions of unit length). So to summarize, if this λ_1 is to be used, it have to be known that T_1 in the experimental data of [Ste72] is conducted at $T_1 = 300K$.

In short the work of [Ste72] part 1, is as follows: The main goal was to determine inter-molecular potential parameters for different potential models; Lennard-Jones and EXP-6, through shock profile comparisons. (The potential will be somewhat analog to viscosity in a *continuum* model). An experimental density profile is obtained through 5 runs of shocks in Argon (it is also performed for Krypton, Xenon,

Neon). Then, DSMC (Direct Simulation Monte Carlo) is performed, with Lennard-Jones potential model and for EXP-6 potential model, and the parameters adjusted to best fit the experimental curve. These parameters (ϵ, k) are given explicitly and a temperature relation is given as

$$T^* = \frac{kT}{\epsilon} \qquad Inter-Molecular\ Potential\ Well\ Depth \qquad (2.11)$$

The $T^* = \frac{kT}{\epsilon}$, for each gas is determined when the Monte Carlo profile matches the experimental one. The variable T is the experimental temperature. So it is, in principle, possible to determine the experimental temperature through this formula. But this introduces uncertainty since to achieve the best fit of T^* the statistical scatter (from DSMC) have to be made as small as possible. It is stated in [Ste72]: "No way is known to remove the expected statistical scatter and thus find the true density.". It does not get better when he concludes that: " Finally, a conclusion, which applies to all rarefied flows, is that the shock structure method is an ineffective way to determine the shape of the potential well (i.e. the attractive forces)...". Therefore, in this thesis, the idea of finding the temperature and use the real physical parameters is abandoned. A completely non-dimensional-furnished set of equations is used for numerical calculations instead.

Further still, the experimental data from [Ste72] are normalized and adapted to fit the numerical simulations of the aforementioned Monte Carlo simulations (not the other way around). This, will affect the normalization procedure herein to most correctly fit the data, see Section 2.3.6.

Note: The subsequent section explaining the normalization, Section 2.3.6, also make use of the "*" notation. This is however not connected to T^*. It is merely a coincidental result of being consistent with the notation in [Ste72] in this subsection.

2.3.3   Non-Dimensional Form

The lack of the complete raw data presents the opportunity to let the problem enjoy the benefits of non-dimensional form. The scaling is inspired by [GR07]. The variables will be scaled by a value at a chosen reference state. The upstream state, denoted by 1, is chosen as reference, as is the common practice for shock structure problems. The following variables are specified freely in the most convenient manner

$$T, \quad p, \quad c, \quad \mu \qquad (2.12a)$$

Keeping

$$Pr = 2/3, \quad and \quad \gamma = 5/3 \qquad (2.13a)$$

constant, then, to not over-determine the system the following must be scaled with dependence from the above

$$\rho, \quad x, \quad R, \quad \kappa, \quad c_p, \quad c_v \qquad (2.14a)$$

A preferable scaling of x, is one that does not change its size, i.e., keeping it as close to 1 as possible. This enables a direct "overlap" of the experimental x-axis and the

one obtained here. Said differently, obtaining a scaling such that $\lambda = 1$ implies that one unit length of the axis in the simulations equals one unit length of the x-axis for the experimental values. Therefore, it is desirable that

$$\overline{x} = \frac{x}{\lambda} \approx x \tag{2.15}$$

That is $\lambda \approx 1$. Overbar denotes the non-dimensional/scaled variable.

The natural λ is the molecular mean free path upstream

$$\lambda_1 = \frac{16}{5\sqrt{2\pi\gamma}} \frac{c_1 \mu_1}{p_1} \tag{2.16}$$

It is readily seen that $\frac{16}{5\sqrt{2\pi\gamma}} = 0.99 \approx 1$. Now, since c, p, μ are chosen freely, they can be conveniently set

$$c_1 = 1, \quad \mu_1 = 1, \quad p_1 = 1 \tag{2.17a}$$

to achieve the desired scaling of $\overline{x}$. In addition, $T_1 = 1$ is chosen.

The following non-dimensional forms are now employed

$$\overline{T} = \frac{T}{T_1}, \quad \overline{p} = \frac{p}{p_1}, \quad \overline{R} = \frac{c_1^2}{\gamma T_1}, \quad \overline{\mu} = \frac{\mu}{\mu_1} \tag{2.18a}$$

Yielding $\overline{R} = \frac{3}{5}$. The remaining parameters are determined through the following

- ρ_1 is computed via the ideal gas law: $\rho_1 = \frac{p_1}{RT_1}$

- The Mach Number M_1 on the upstream side, is the supersonic Mach number, i.e. $M_1 = 8$

- Then, $u_1 = M_1$, since $c_1 = 1$

- $T_2, P_2, M_2, \rho_2, u_2$, can subsequently be determined by the Rankine-Hugoniot relations(1.21), (1.22), (1.23), (1.24) where needed

- The value of c_p also has to be scaled since the Prandtl number is constant equal to $2/3$. The relating equations of c_p and c_v are

$$R = c_p - c_v, \quad \gamma = \frac{c_p}{c_v} \tag{2.19a}$$

Since $\overline{R} = 3/5$ and $\gamma = 5/3$, it is easy to show through simple substitution of c_v that $\overline{c_p} = 3/2$. The Prandtl number relation gives

$$\overline{\kappa} = \frac{\overline{c_p}\, \overline{\mu}}{Pr} = \frac{9}{4}\overline{\mu} \tag{2.20}$$

By this procedure the Navier-Stokes equations and the Eulerian model do not have to be changed from their original form when computed. Rather, the boundary conditions, together with $\overline{R}$ and $\overline{c_p}$ sets the non-dimensional scene in place. Note that $\mu_1 = 1$ is merely used to scale the x-axis. Once this is done, the unit length of the x-axis stays fixed for all simulations. The values of μ will vary for the different simulations and its effect is to thicken/thin the shock [Kun16].

2.3.4 Boundary and Initial Conditions

This problem has fixed far field boundary conditions with supersonic inflow- and subsonic outflow conditions. The boundary conditions are given by the Rankine-Hugoniot relations (1.21),(1.22),(1.24). Far upstream and downstream all gradients vanish.

The correct number of boundary conditions, as shown in [SCN07] for Navier-Stokes, is given below in Table 2.1. For the Eulerian model, there is also a diffusive term in the conservation of mass equation, therefore an extra boundary condition is needed [Sva18].

Table 2.1: Number of boundary conditions for 1-dimensional supersonic inflow and subsonic outflow

	Supersonic Inflow	Subsonic Outflow
Navier-Stokes	3	2
Eulerian Model	3	3

The boundary conditions given below in Table 2.2 were used and produced stable simulations

Table 2.2: Specified Boundary Conditions for the conservation of mass, density and energy equations. Computed via the Rankine-Hugoniot Relations

		Supersonic Inflow	Subsonic Outflow
Navier-Stokes	Mass	ρ_1	
	Momentum	m_1	m_2
	Energy	E_1	E_2
Eulerian	Mass	ρ_1	ρ_2
	Momentum	m_1	m_2
	Energy	E_1	E_2

Generally for a given boundary accuracy of a, a nodes on each boundary are modified in the SBP-stencils [Gus08]. The SBP operators used herein are second order accurate for the interior nodes and first order accurate at the boundary. The outermost nodes therefore have to be modified. The simplest way to employ this is by the injection method, that is, overwriting/injecting the fixed values onto the outermost nodes.

To start the simulation initial values for the variables are needed. The initial conditions are simple step functions where the boundary values are extended to cover each half of the domain.

2.3.5 Viscosity Model

Modeling viscosity is of paramount importance as it leads to quite substantial differences in the density profiles (as is seen in Chapter 3). The power-law viscosity

model is suited for the Navier-Stokes equations, given again here as

$$\mu = AT^r, \quad 0.5 < r < 1 \tag{2.21}$$

for some constant A. Most real gases fall in the range of $0.64 < r < 1$ [GR07].

Now, the Eulerian kinematic viscosity is

$$\nu = \alpha \frac{\mu(T)}{\rho(x,t)} \tag{2.22}$$

Let, for this subsection, the subscript E and NS, denote Eulerian and Navier-Stokes, respectively. It is readily seen that one can achieve $\nu_E = \mu_{NS}$, at some point *if*, μ_E is kept constant but scaled according to (2.18). This naturally begs the question if this dependency is enough, i.e. using constant dynamic viscosity μ_E, for the Eulerian kinematic viscosity? However difficult to compare the "function" of ν in Eulerian model to the function of μ in Navier-Stokes, this idea will be pursued in the simulations. Letting μ_E follow the same power law as the Navier-Stokes equations is also simulated for.

Another way to justify this idea is to differentiate the following

$$\frac{\partial \mu_{NS}}{\partial r} = Ar \frac{1}{T^{1-r}} \tag{2.23}$$

and, keeping μ constant for Eulerian

$$\frac{\partial \nu}{\partial \rho} = -\alpha \frac{\mu_E}{\rho^2} \tag{2.24}$$

One can say that the *rate of temperature dependency* is decreasing in both cases.

Svard also propose two different values for α, namely, $\alpha = 1$ and one in accordance with the viscosity coefficient in Navier-Stokes equations; $\alpha = 4/3$. Both was simulated for, and a suggestion for which constant is the more proper one is stated in Chapter 5.

To determine the upper bound on the constant μ, the power law was used as a reference. The downstream temperature value is the highest one, i.e. T_2 given by the Rankine-Hugoniot relation (1.24)

$$T_{max} = T_2 \quad \implies \quad \mu_{max} = A(T_{max})^r \tag{2.25}$$

Now, setting $A = \gamma^r$ and $r = 0.81$,

$$T_{max} \approx 21 \quad \implies \quad \mu_{max} = (1.67)^{0.81}(21)^{0.81} \approx 17.8 \tag{2.26}$$

So the range of the dynamic viscosity in this work is

$$1 \leq \mu \leq 17.8 \tag{2.27}$$

However, the simulations shown with constant dynamic viscosity, were done well within in the limits with $\mu \leq 10$. Worse approximations and instability arose above this.

For the Sutherland viscosity law, the constant C_1 needed to be defined. Using again that $T_{ref} = 1$ and $\mu_{ref} = 1$ and testing by trial and error. The largest Sutherland temperature value $S_u = 2$ was used, giving

$$C_1 = \frac{\mu_{ref}}{(T_{ref})^{3/2}}(T_{ref} + S_u) = 3 \tag{2.28}$$

Then stable simulations were done with

$$\mu = \mu_{ref}C_1\frac{T^{3/2}}{T + S_u} \tag{2.29}$$

The lower value of S_u was equal to 0.9, and again determined by test simulations. Below this value was no point of doing due to poor fit of the simulated data with the experimental. So to summarize for the application of Sutherland's viscosity law

$$0.9 \leq S_u \leq 2 \tag{2.30}$$

Note that for $S_u = 2 \implies \mu \approx 12.6$. To achieve this with the power law one would need that

$$r \approx 0.83 \tag{2.31}$$

2.3.6 Normalization and Fitting of Data

One issue that need to be addressed is the normalization of the numerically calculated data. The experimental data from Steinhilper [Ste72], has upstream and downstream endpoint values for the density; $\rho = 0.001$ and $\rho = 1.009$, respectively. He defines the point $x = 0$ to be associated to the value $\rho^* = \frac{\rho-\rho_1}{\rho_2-\rho_1} = 0.5$. It is unclear why this boundary-data is so. It might be because of the fitting procedure, or it might be because of the experiment is run at *about* Mach-8, as he writes. Then if Mach-8 is used as an exact value in the Rankine-Hugoniot relations, a small deviation in the normalized data will occur. That is, assuming direct density measurements at the far upstream and downstream were not done. Although the endpoints having quite a small deviation from 0 and 1, a linear scaling term to match the endpoints properly is added herein.

$$\rho^* = \frac{\rho - \rho_1}{\rho_2 - \rho_1} + (0.001 + \frac{x}{L}0.008) \tag{2.32}$$

Where L is the length of the domain and $0 \leq x \leq L$. See Appendix B for the experimental data from [Ste72]. Furthermore, as is common in shock experiments, the numerically obtained graphs are shifted so that $\rho^* = 0.5$ corresponds to the point $x = 0$, see for example [Als76] or [RD19]. However, since the value is not predefined (only boundary conditions are), the value closest to $\rho^* = 0.5$ is associated with $x = 0$, after the simulation has converged.

2.3.7 Tolerance

The standard L_2 norm was used as a measure on the density for two consecutive time steps. The size of the tolerance depends on the time step, and by some trials it was found that $TOL = 5 \cdot 10^{-6}$, was a reasonable tolerance. That is, the simulations stopped when

$$\left\| \boldsymbol{\rho}^{(k)} - \boldsymbol{\rho}^{(k+1)} \right\|_2 < TOL \tag{2.33}$$

Where k denotes the timestep. No changes in the shock structure were observed below this (in some test simulations).

Chapter 3

Results

3.1 Results

First of all, note that the raw data from [Ste72] has its x-domain from [-8, 7]. Since it is not straight forward how to employ this, the resulting figures need a little justification. In [Ste72], the experimental data are shifted to match the DSMC (Direct Simulation Monte Carlo) not the other way around, and relocated such that x = 0 corresponds to the normalized value $\rho^* = 0.5$. This shift must be done since the exact location of $\rho^* = 0.5$ in the original profile, stemming from the measurement of the *stationary* electron gun, is not known in advance due to the lack of no absolute coordinate.

It is not stated explicitly why the domain is not symmetric, [-8, 8] or [-7,7], but from reading the thesis of [Ste72] it seems like the original axis spanned from $[-7.5, 7.5]$ and due to the shift ended up as $[-8, 7]$

A shift of the shock profile such that the value closest to $\rho^* = 0.5$ was relocated at x = 0, were done for all simulations.

The uncertainties for the experimental values are addressed in Section 4.1. However, the main point is stated here in advance. Steinhilper does not address the uncertainties to his experimental procedure, however, Alsmeyer do in [Als76] for his experimental data. Even though there are some differences between the two experiments (e.g size of the tube is 150mm diameter in Alsmeyer opposed to 432 mm in Steinhilpers experiment), the best one can do is to hope for a similar uncertainty. Alsmeyer states that the total uncertainty for the density profiles are ±4% but believed to be accurate within ±1%. In the subsequent figures, the circles marks the experimental data, and the extent of the circles is slightly larger than ±1%. For aesthetic reasons these circles are used instead of error-bars. The ±4% error-bars was after contemplation left out. They were only seen to clutter the figures and not add valuable information.

3.2 Simulations

3.2.1 Constant Dynamic Viscosity

Note that for all following subsections presenting the results the structure is the same. The first figure shows Eulerian model with $\alpha = 1$. Then comes Eulerian model with $\alpha = 4/3$ followed by Navier-Stokes. In the descriptive labels in the top-left corner, resides the viscosity information.

In this subsection all the figures presented are simulations where the dynamic viscosity, μ, was kept constant. The viscosity values are scaled as explained in Section 2.3.3. Note that for all figures on the density profile, the normalized density, as explained in 2.3.6, is plotted against the x-axis whose units are given in mean free paths.

For values of $\mu > 10$, slow or non converging results emerged from the Eulerian model while instability for the Navier-Stokes. Hence, the maximum value $\mu_{max} = 10$.
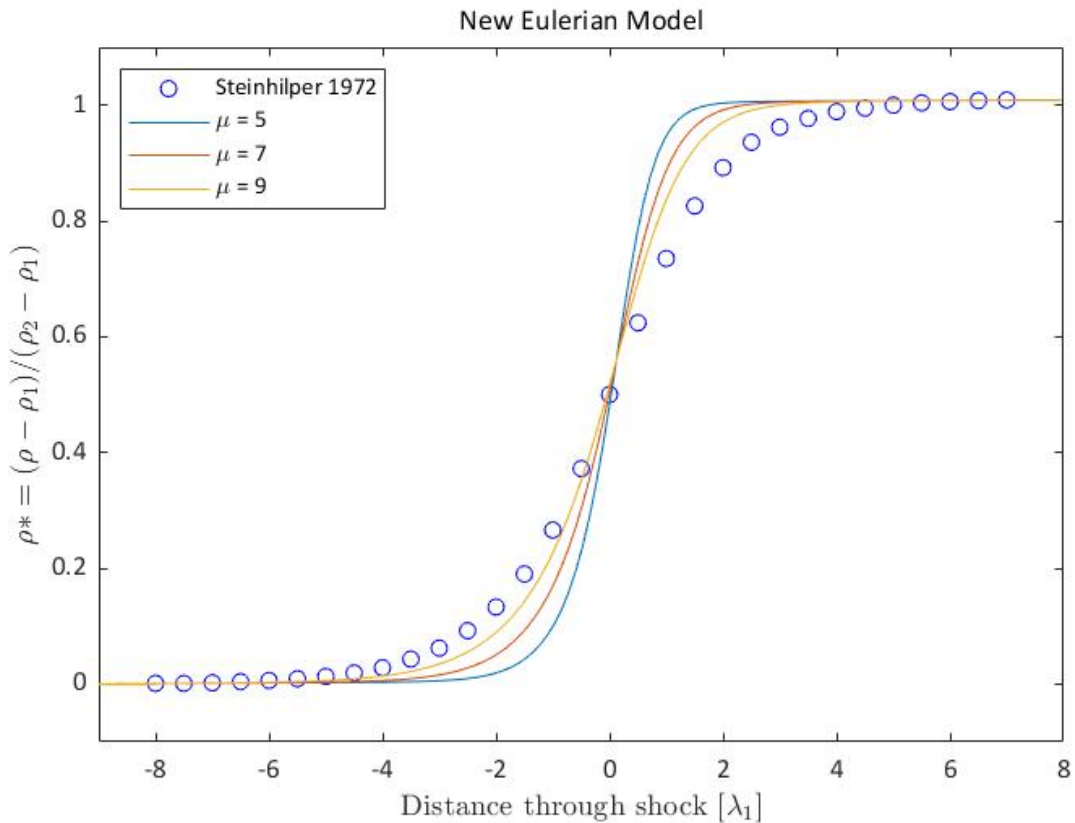
Figure 3.1: Eulerian model with $\alpha = 1$ and constant dynamic viscosity μ values.

The trend in these simulations is clear. The higher the viscosity the closer the simulated values approach the experimental values, but still, all curves are poor approximations.

In the following plot, Figure 3.2, $\alpha = 4/3$ but the same viscosity values are used to compare with the $\alpha = 1$ case above.
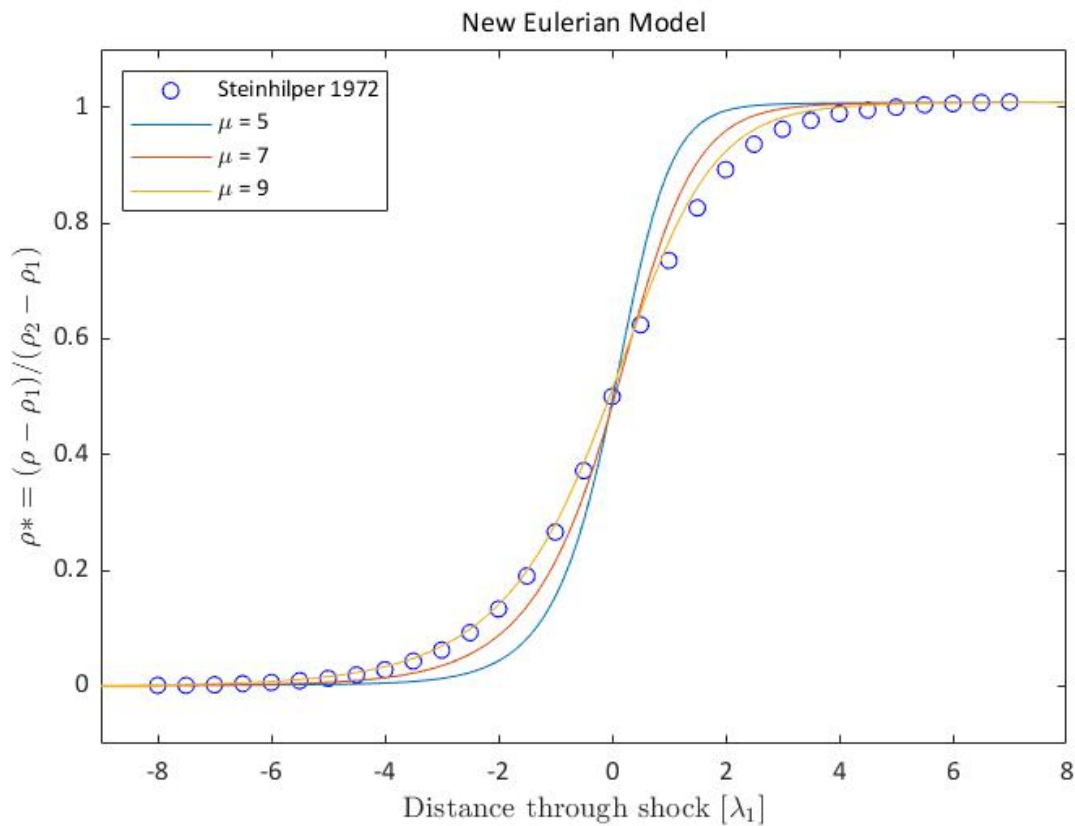

Figure 3.2: Eulerian model with $\alpha = 4/3$ and constant dynamic viscosity μ values.

The trend in these simulations is the same, as expected. The higher the viscosity the closer the simulated values approach the experimental values. However, these curves are better approximations. The curve for $\mu = 9$ follow quite tightly in the left part, then overshoots a little just right of the middle before hitting close to exact values near the boundary.

In light of the two previous results, one would be encouraged to tune the viscosity around $\mu = 9$ to obtain closely fitting curves. In Figure 3.3 below, the dynamic viscosity was set to $\mu = \{9, 9.5, 10\}$.
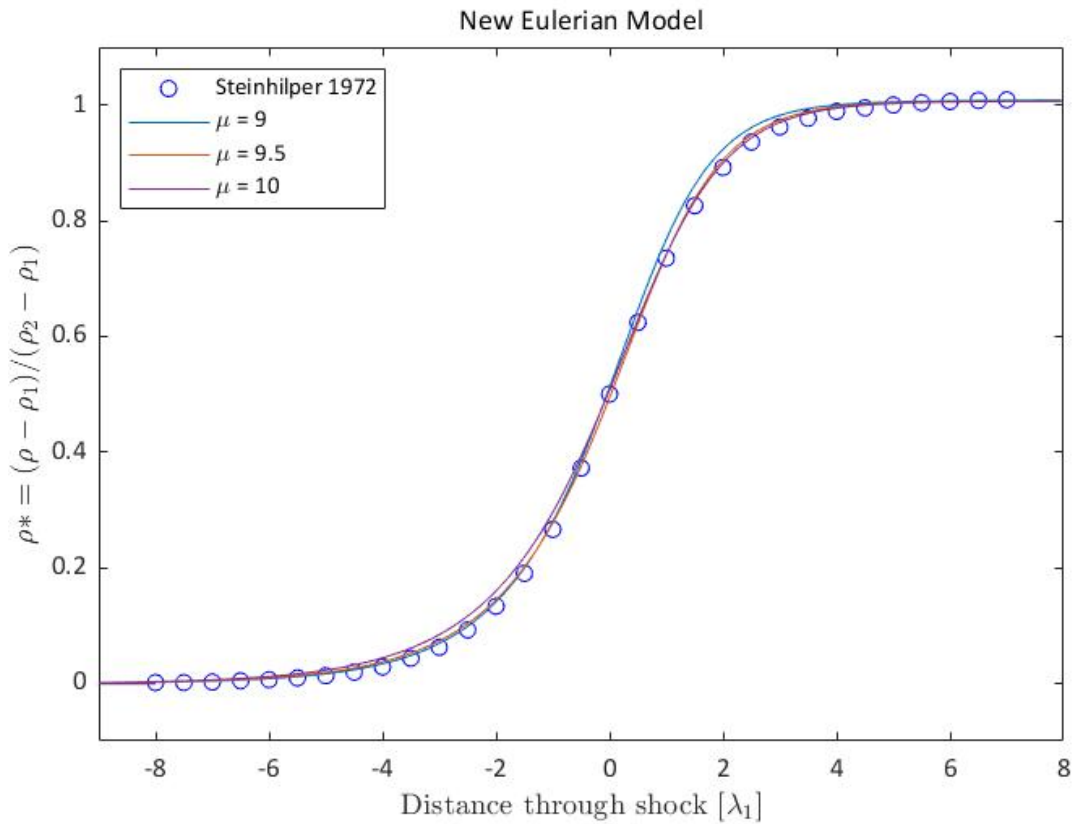

Figure 3.3: Eulerian model with $\alpha = 4/3$ and constant dynamic viscosity μ. The curve with $\mu = 9.5$ seems to be the closest approximation to the experimental values.

Even though hard to see due to overlapping curves, the curve with $\mu = 9.5$ is the compromise of $\mu = 9$ and $\mu = 10$. In the left half, $\mu = 10$ clearly overshoots, while it hits the experimental values neatly in the right half. This is the opposite behaviour of the case $\mu = 9$. For clarity the case of $\mu = 9.5$ i given separately in Figure 3.14 in Section 3.2.5 below. This is the best approximation obtained with the new Eulerian model in this work.

It is well known that constant viscosity lead to poor approximations for the Navier-Stokes equations. For completeness and comparison this is included below in Figure 3.4.
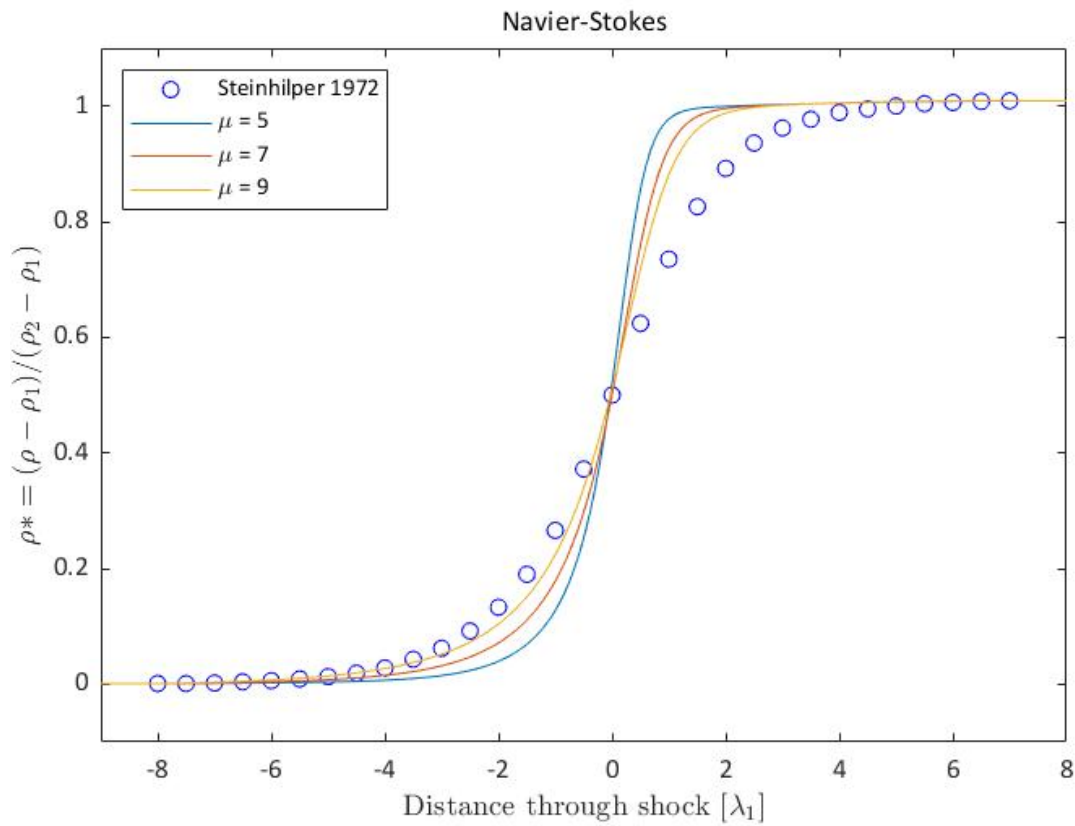

Figure 3.4: Navier-Stokes equations with constant μ.

Clearly a much poorer fit than for the Eulerian model. Still, the trend is the same. The highest viscosity curve is closer than the other two.

3.2.2 Power Law Viscosity Model

In this subsection the simulations for the viscosity model $\mu = T^r$ are presented. The descriptive labels in the top left corner gives the value of the exponent.

The following plot 3.5, shows the Eulerian model with 4 different exponent values. Three of them suggested by [GR07] and the value of $r = 0.81$ from [ESM05].
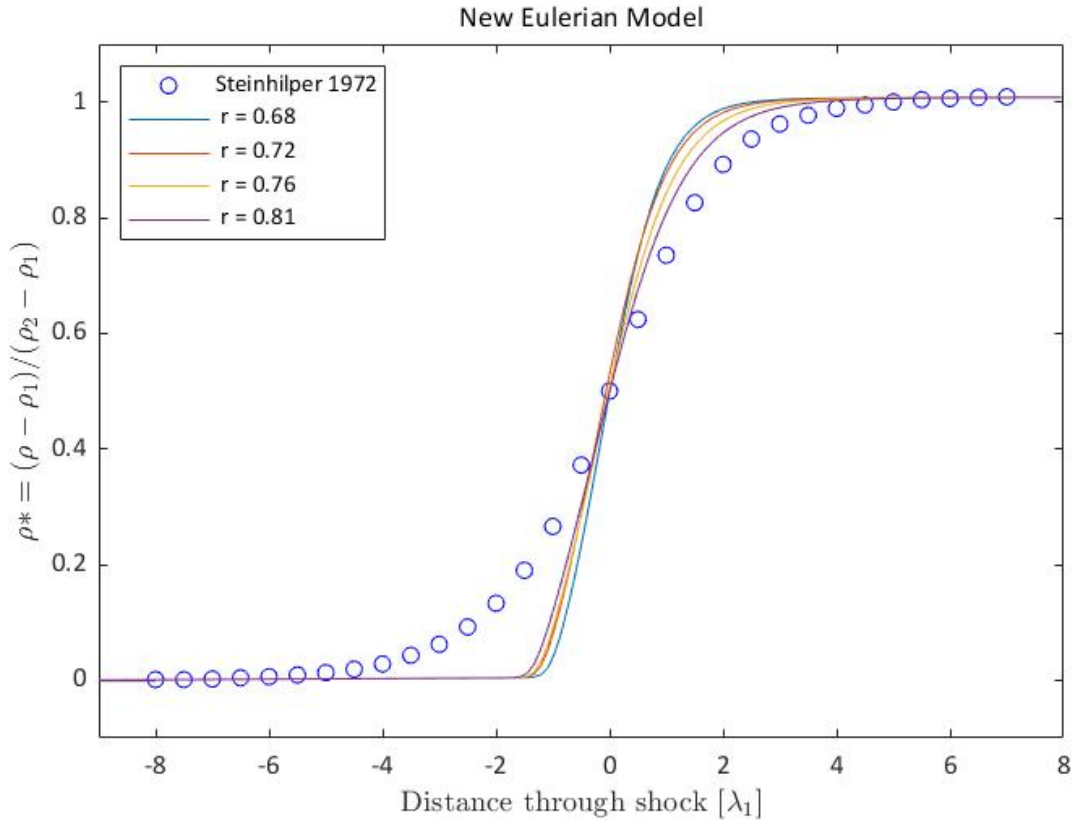

Figure 3.5: Eulerian model with $\alpha = 1$ and viscosity $\mu = T^r$

Clearly this power law fails for the case of Eulerian model with $\alpha = 1$.

In Figure 3.6 below, the same four cases of $r = \{0.68, 0.72, 0.76, 0.81\}$ are plotted, but now for $\alpha = 4/3$.
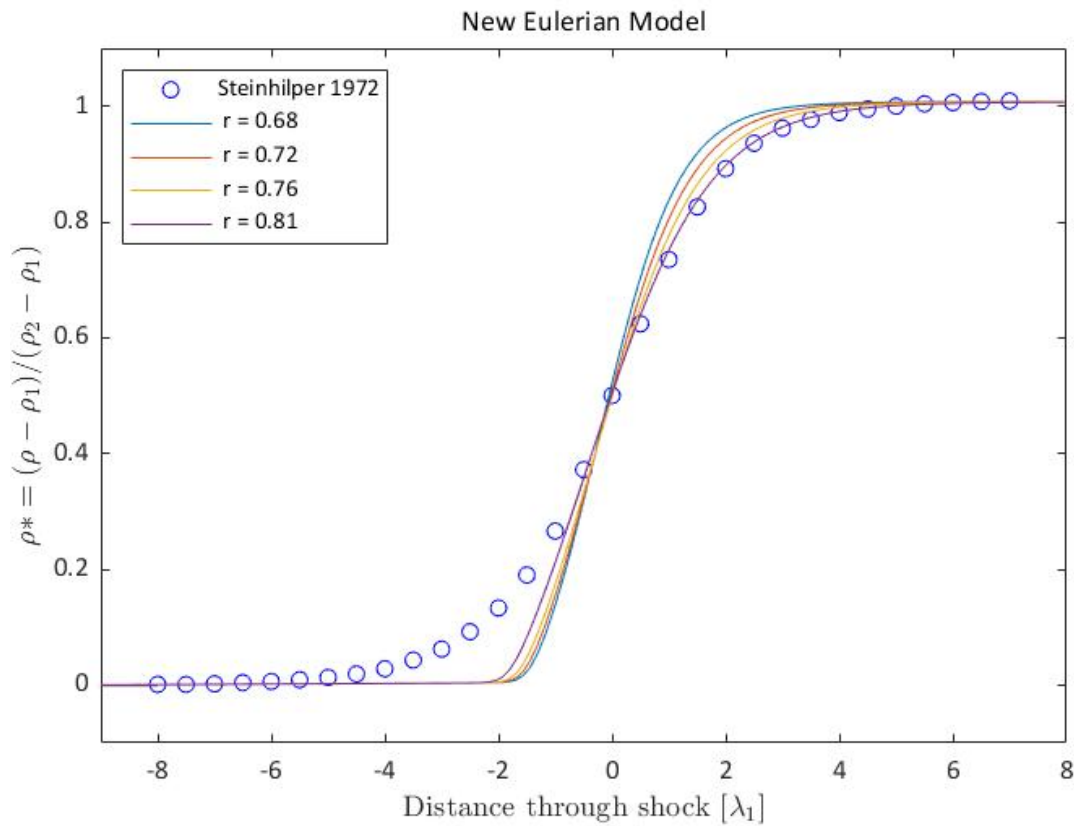

Figure 3.6: Eulerian model with $\alpha = 4/3$ and viscosity $\mu = T^r$

This also are poor approximations compared to the constant viscosity cases. The main difference is that the power law gives no curvature to the left of -2 on the x-axis, where a dramatic "kink" emerges. However, for the case of $r = 0.81$ there is a very good approximation for the right half part. Again, one can say that $\alpha = 4/3$ gives better results than $\alpha = 1$.

One important observation is that this "kink", is also seen in Brenner's modified Navier-Stokes equations when applied to a similar shock structure problem. See [GR07] for this.

In Figure 3.7, the values for $r = \{0.68, 0.72, 0.76, 0.81\}$ for the Navier-Stokes equations are shown. Note that for the values $r = \{0.76, 0.81\}$, the time step needed to be halved, due to growing oscillations. The halving of time-step resolved the instability. The instability emerged from the high viscosity end of the domain, i.e. the right part/downstream.
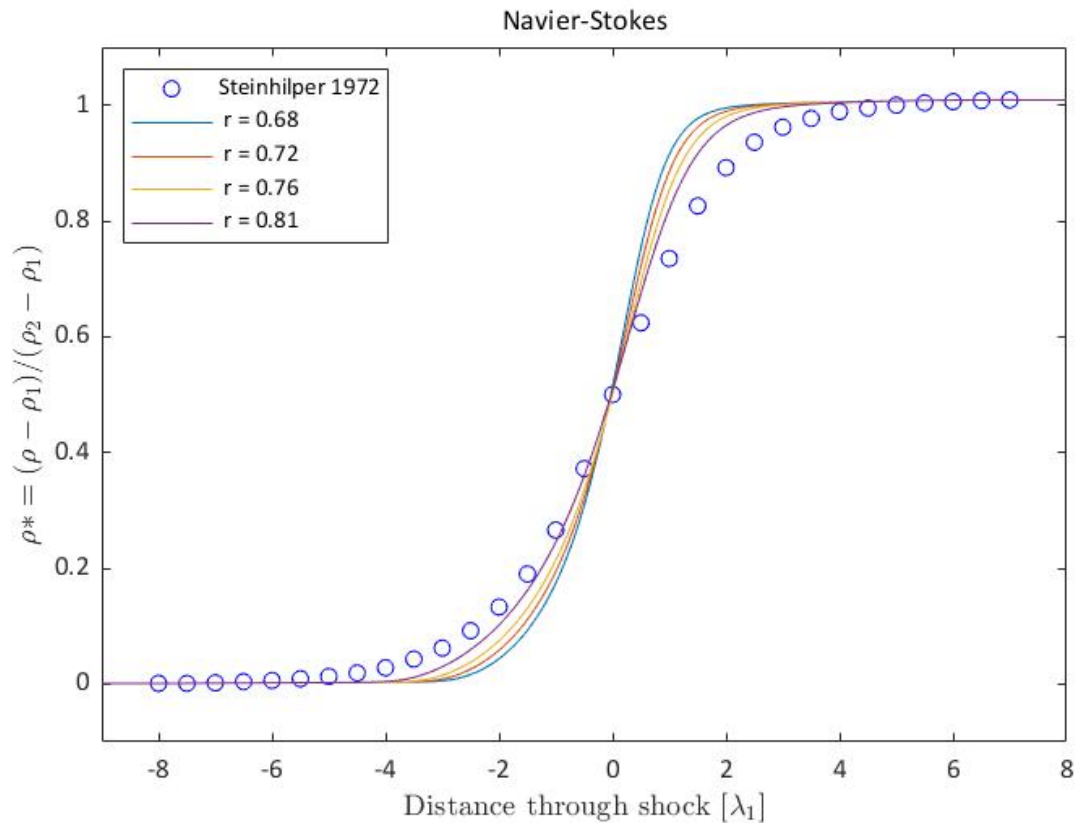

Figure 3.7: Navier-Stokes with the viscosity model $\mu = T^r$

For this power law it is obvious that Navier-Stokes perform a lot better than the Eulerian model. The characteristic "kink" is not seen here, rather a more "smooth" curvature all through the domain.

3.2.3 Power Law Viscosity with Coefficient

In this subsection simulations with the power law $\mu = \gamma^r T^r$ are presented. Compared to Section 3.2.2 above, the resulting viscosity is higher with the coefficient γ^r. As an example, if $r = 0.72$, then since $\gamma = 5/3 \implies \mu \approx 1.45 T^r$, a significant difference.

In Figure 3.8 the Eulerian model with $\alpha = 1$ is presented.
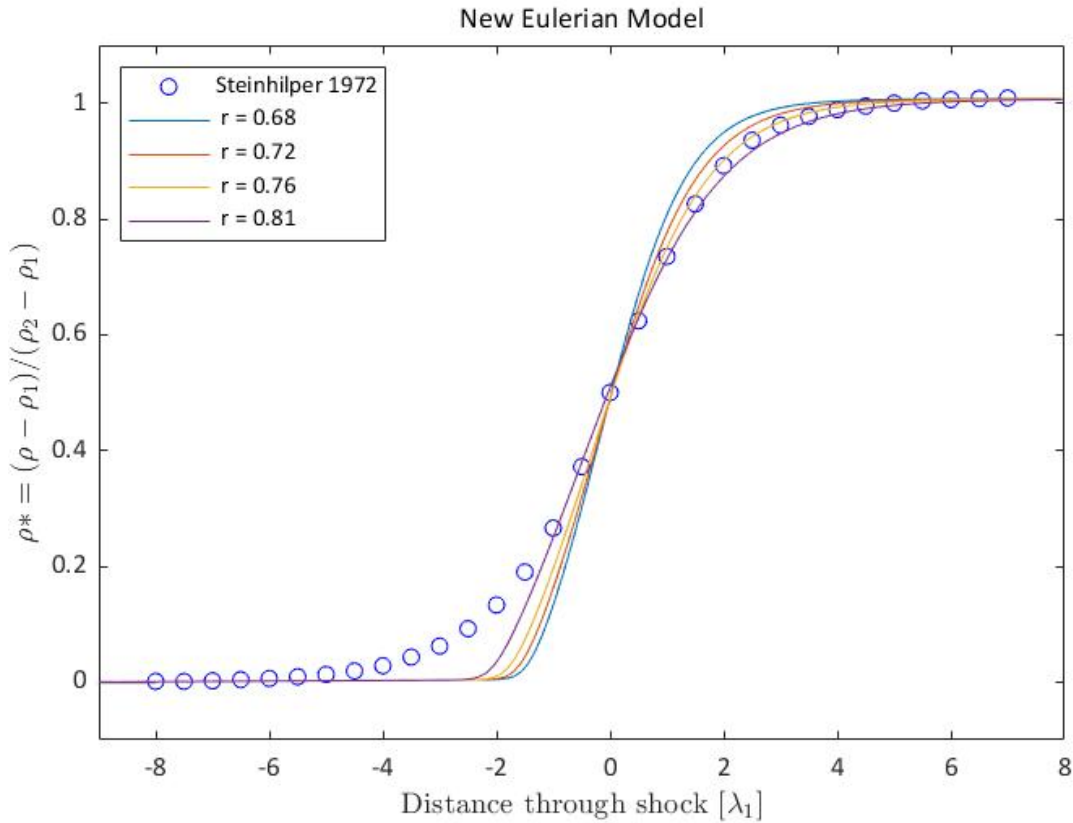

Figure 3.8: Eulerian model with $\alpha = 1$ and $\mu = \gamma^r T^r$

The result have the same trend as in Figure 3.5 with the sharp transition from flat to steep curve at around $x = -2$. However, the transition is softer here owing to higher viscosity, and therefore a better approximation.

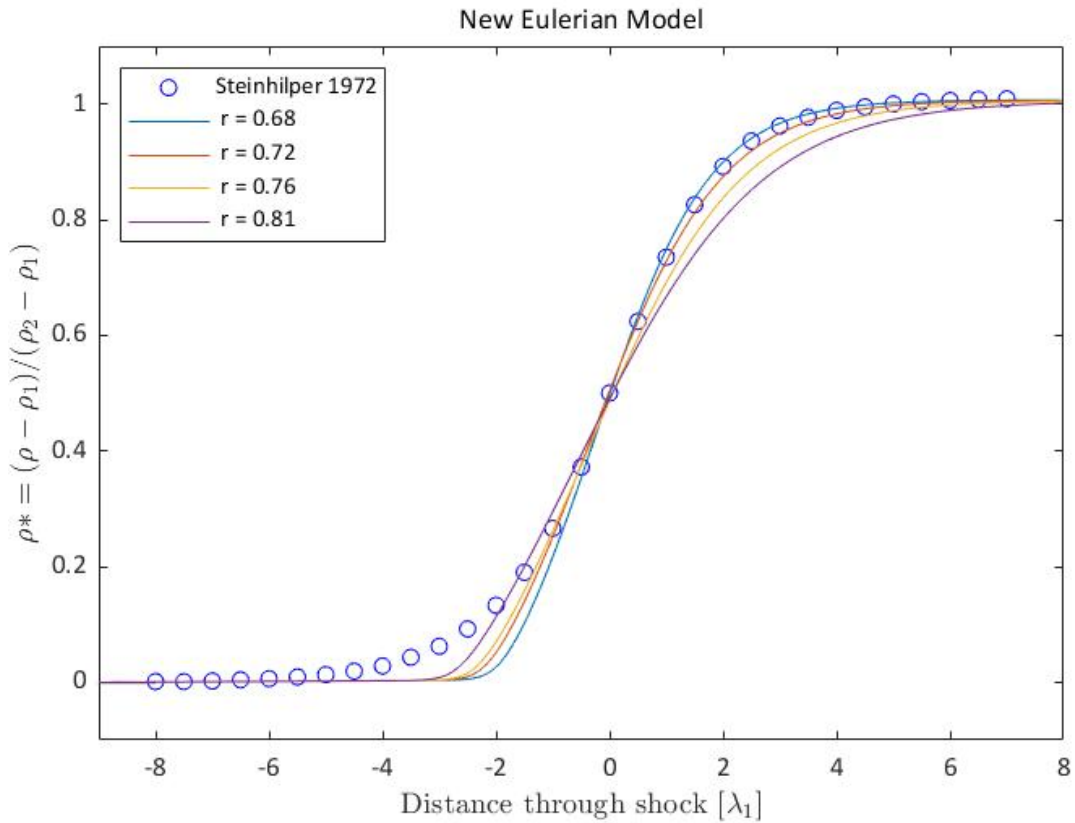In Figure 3.9 the Eulerian model with $\alpha = 4/3$ is presented.

Figure 3.9: Eulerian model with $\alpha = 4/3$ and $\mu = \gamma^r T^r$

Here it is clear that for the highest r values the viscosity is too strong and the curves are well below the experimental values in the right half part. For $r = \{0.68, 0.72\}$ the approximation is only deviating from the 1% (i.e. not touching the circles) in the interval $x = [-4.5, -1]$. Once again it can be stated that the Eulerian model with $\alpha = 4/3$ perform better than with $\alpha = 1$.

The simulations for Navier-Stokes are shown below (Figure 3.10). Note that for $r = 0.81$ convergence was not achieved due to instability and therefore not shown.
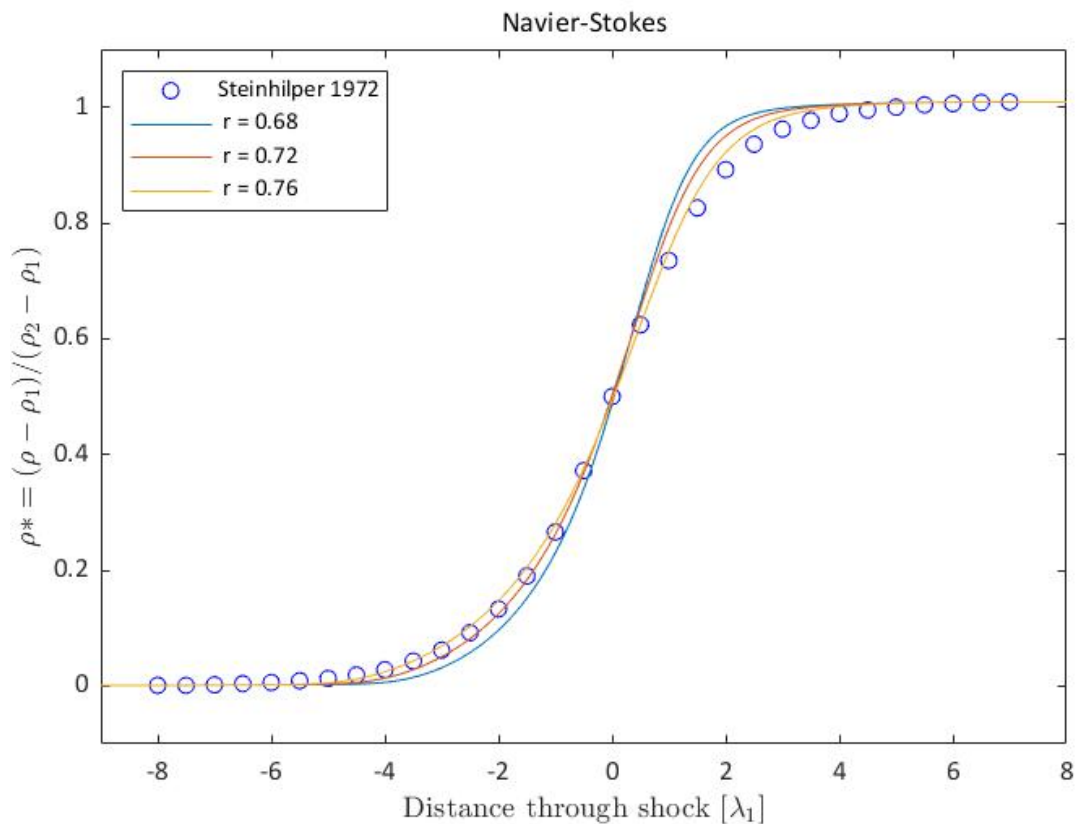

Figure 3.10: Navier-Stokes with dynamic viscosity $\mu = \gamma^r T^r$

The Navier-Stokes perform well for the case $r = 0.76$. Only in the interval $x \approx [2, 3]$ is it not within the 1%. This is the best approximation achieved for the Navier-Stokes equations in this thesis.

3.2.4 Sutherland's Viscosity Law

In this subsection the simulations using Sutherland's viscosity law is shown. The values of the scaled Sutherland temperature are $S_u = \{0.9, 1.3, 1.5, 2.0\}$ and given in the top-left corner of the figures. Some quick comments can be made

- Eulerian model with $\alpha = 4/3$ perform better than for $\alpha = 1$

- The same characteristic "kink" is observed for the Eulerian model, leading to poorer results and hence this viscosity model is not well suited

- Navier-Stokes give approximately the same results as for the Power Law, however not as well.

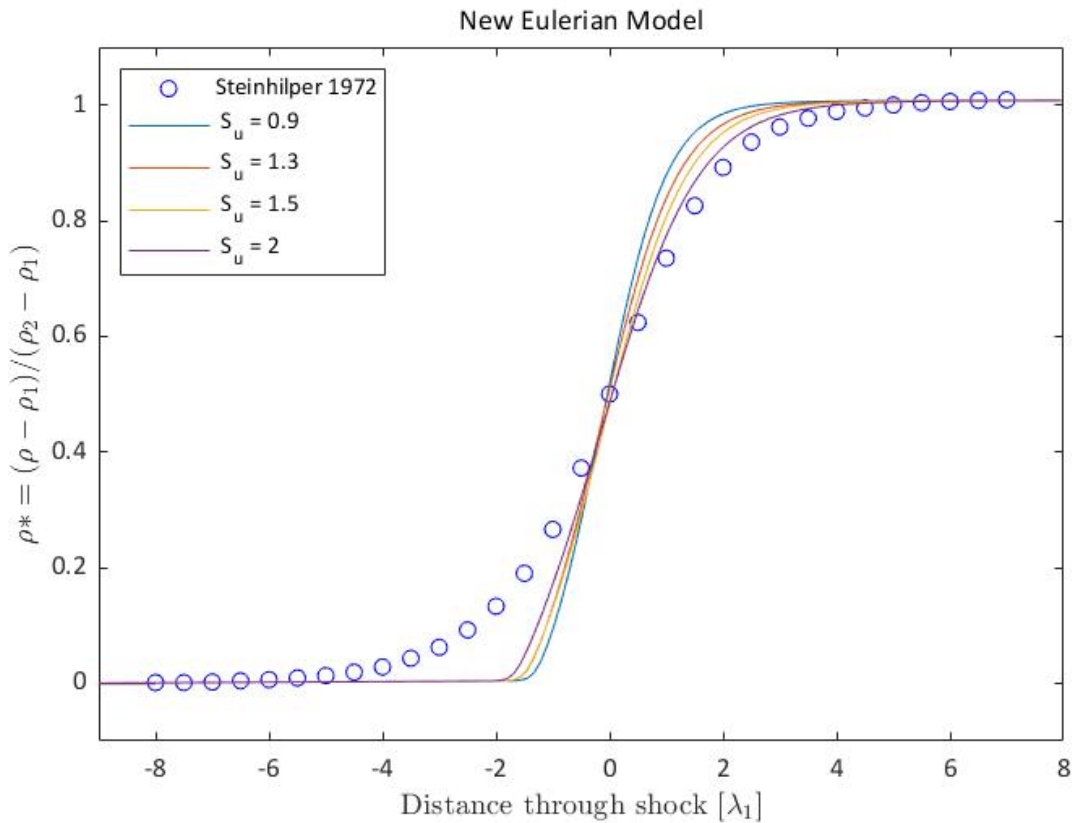The approximations are overall of poorer fit, and for brevity comments on the results are left out.

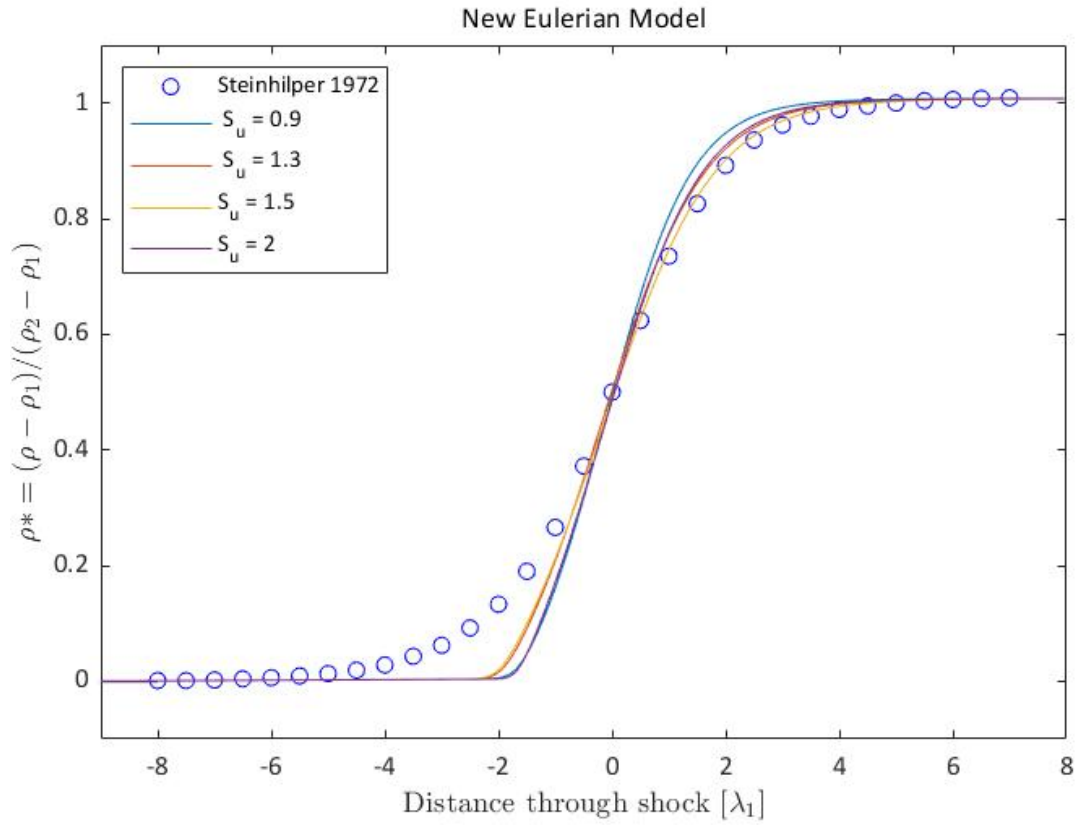Figure 3.11: Eulerian model with $\alpha = 1$ and Sutherland's viscosity law.

Figure 3.12: Eulerian model with $\alpha = 4/3$ and Sutherland's viscosity law.
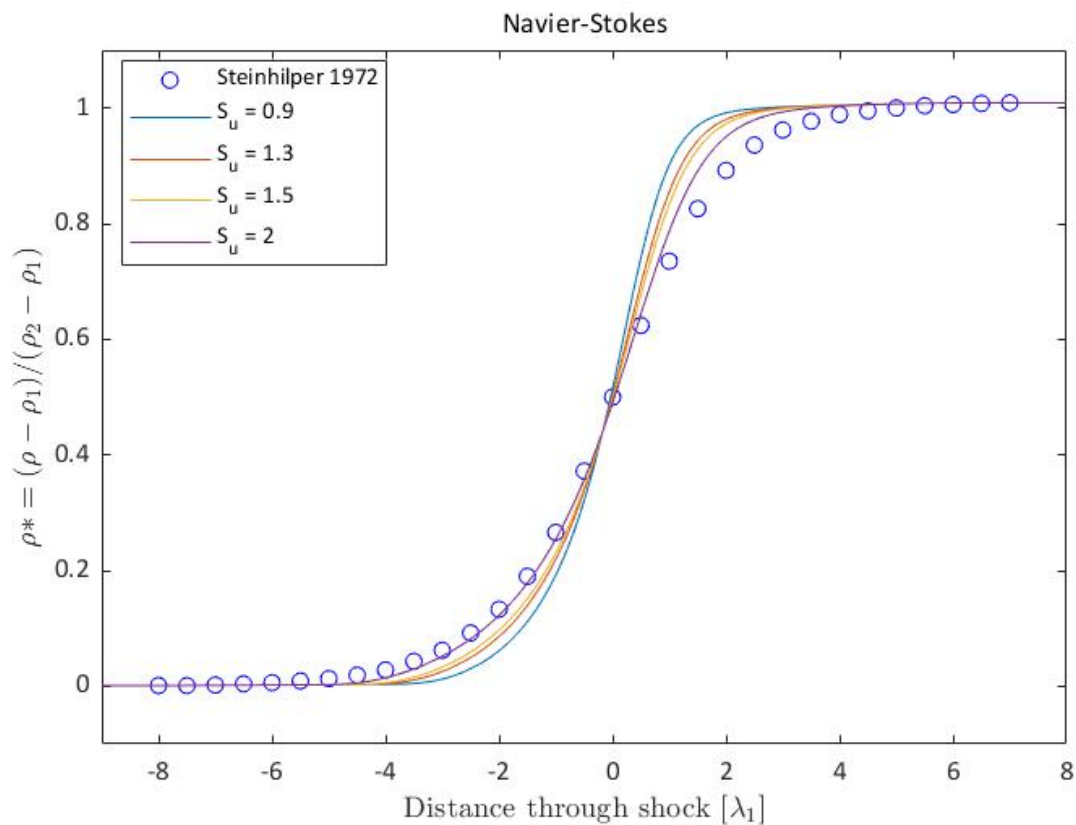
Figure 3.13: Navier-Stokes with Sutherland's viscosity law.

3.2.5 Best Fit Comparison

In this subsection the best fitting curves for the Eulerian model and the Navier-Stokes are given. This gives a clearer picture of the most important results.

From all the plots presented so far it should be clear that too little viscosity yield simulated values below the experimental data for $x < 0$, and simulated values above the experimental data for $x > 0$. This is also observed in the subsequent figures in this subsection.

Below in Figure 3.14, the closest approximation for the Eulerian model is shown.
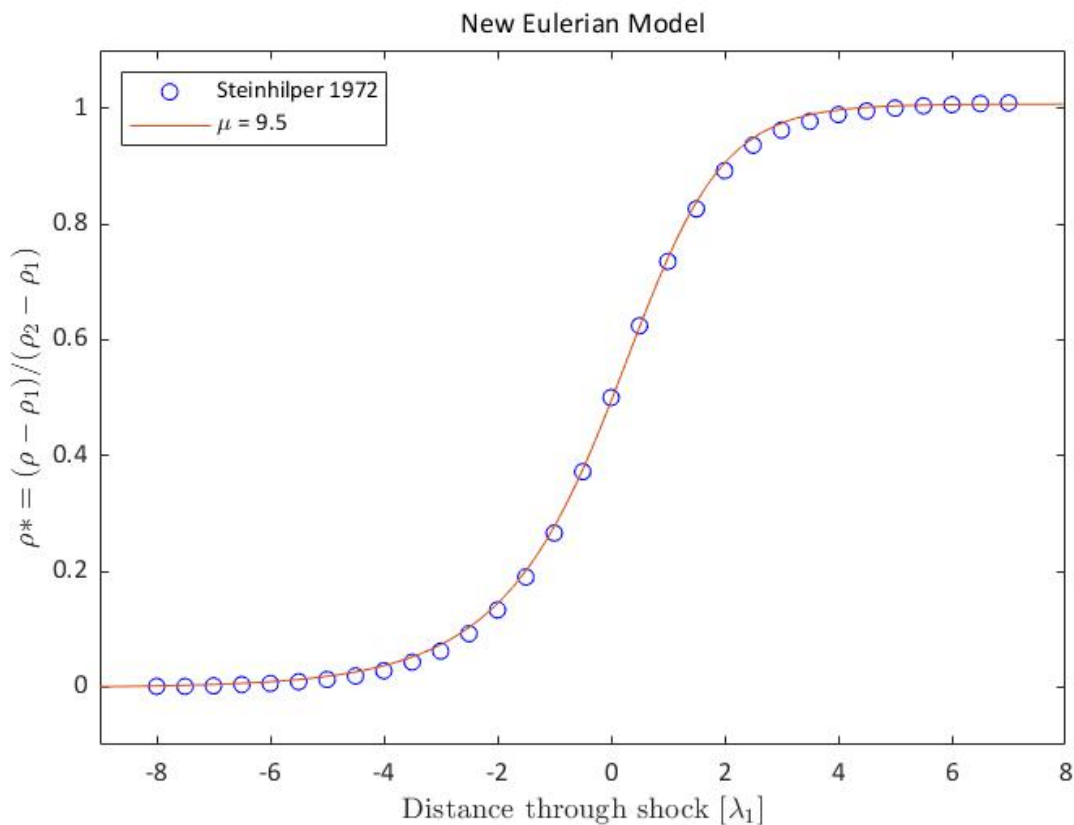
Figure 3.14: New Eulerian model with constant dynamic viscosity $\mu = 9.5$. The closest approximation obtained.

It is readily seen that all the circles are crossed by the simulated curve.

The closest approximation obtained with the Navier-Stokes can be seen in the following plot (Figure 3.15)

Figure 3.15: Navier-Stokes with $\mu = \gamma^r T^r$ and $r = 0.76$. The closest approximation for Navier-Stokes equations.

Only four circles are not crossed by the simulated Navier-Stokes curve.

The closest approximations for the two systems are put together for comparison in the plot below (Figure 3.16).

Figure 3.16: The closest approximations for the two systems.

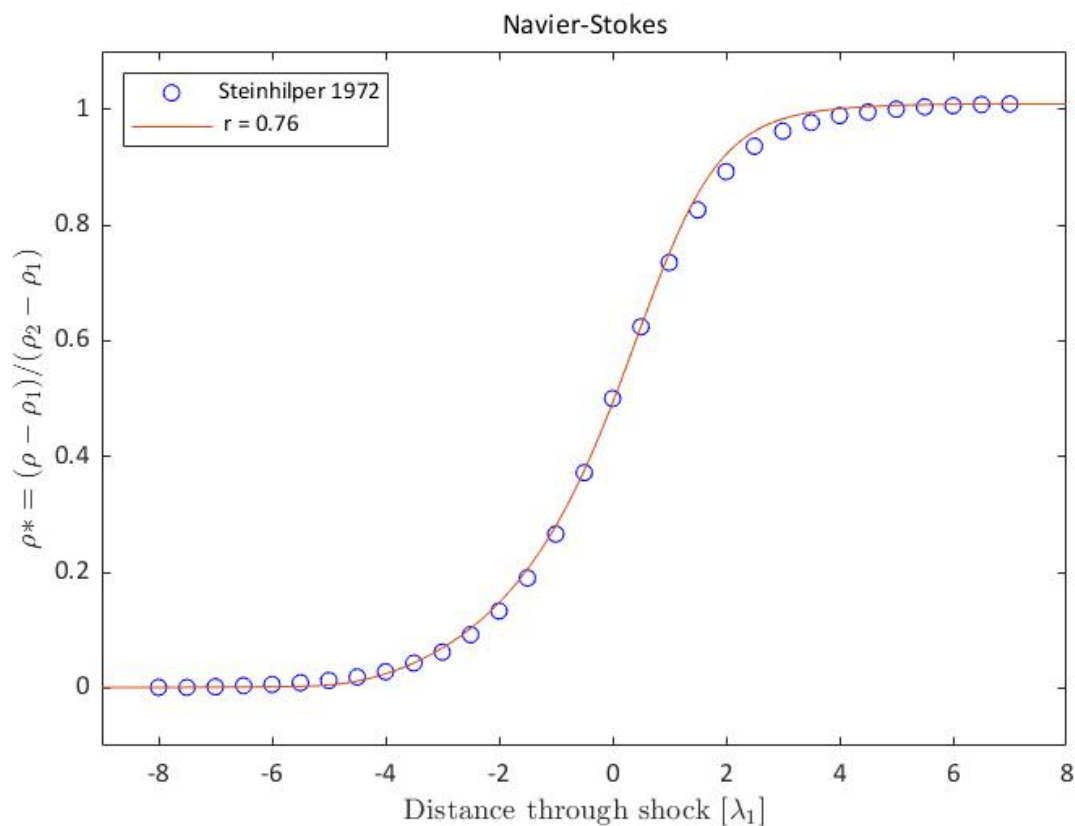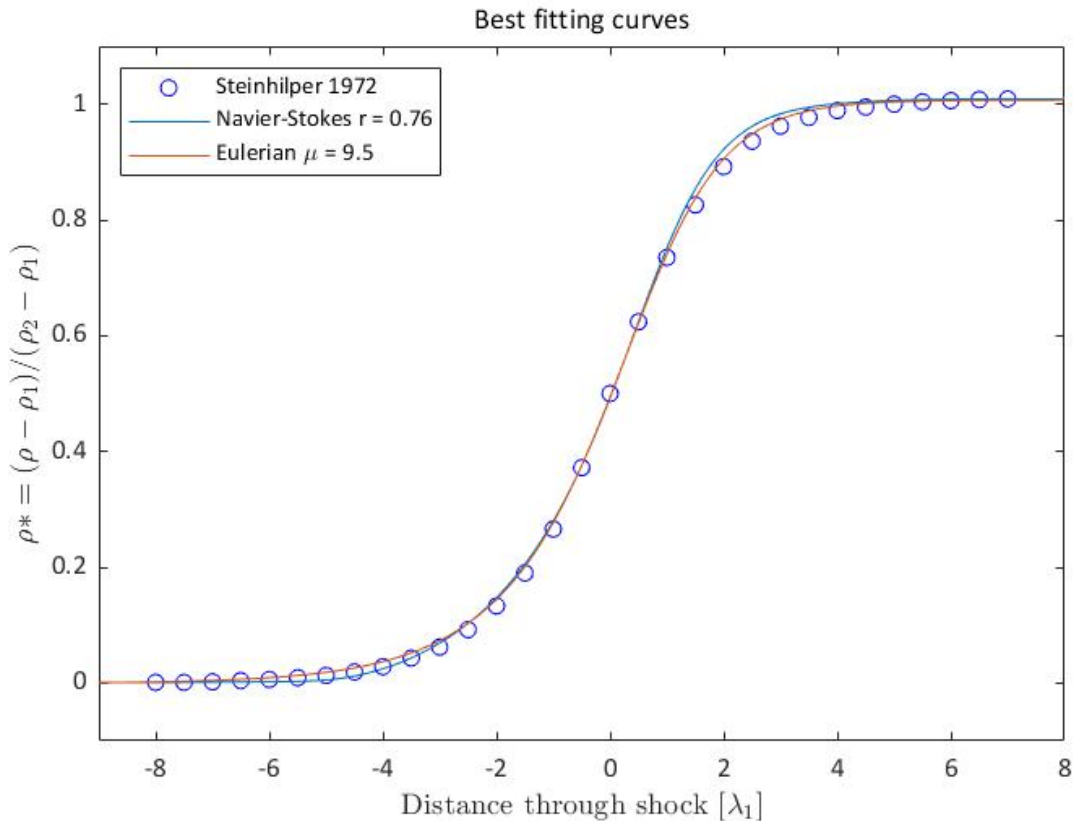It is clear that the two models approximate the experimental values closely. From inspection of the curves it seems that the Eulerian model has a closer fit than the Navier-Stokes. However, one can argue that with tuning of the viscosity parameters one could probably obtain almost identical results. As seen in Figure 3.15, the Navier-Stokes would have needed higher viscosity in the right part and less in the left part to follow the experimental values more closely. An easy way would be to use a slightly lower value than the coefficient γ^r. This reduce the overshoot in left half part. To increase the viscosity in the right half part one would in addition need to use a higher exponent value $r > 0.76$. Since the temperature is almost constant up to where the curvature starts, increasing the exponent has the highest impact in the right half part.

Keeping in mind that the Stokes assumption is employed herein, better results might be achieved with another constitutive relation. However, the higher viscosity might introduce instability, with this numerical method. This could be overcome by adding artificial dissipation, but then more grid points are needed to deal with the added inaccuracy. Using a more proper boundary procedure, such as the SAT method, could possibly kill the eventual instability (See [SN14] for an instructive example of the SAT method effectively killing boundary-induced oscillations, in a Convection-Diffusion equation, as opposed to fixed boundary conditions). Since it is easier to have stable simulations with the Eulerian model, this favors mass diffusion.

3.3 Conservation of momentum

It is interesting to note the difference in momentum. As seen from Figure 3.17 the momentum is constant through the whole domain for the Navier-Stokes, while the Eulerian system has a peak slightly to the left of the center. This is consistent with the findings in [Sva18]. If the simulation is ran further for the Eulerian model, this peak is observed to traverse very slowly. This in turn makes it hard to achieve lower tolerance since the variables at the "peak-affected" area is constantly changing.

For a proper comment on this [Sva18] states that: "Note that momentum is not globally conserved in either of the simulations. It is only conserved up to the point where the solution interacts with the boundary, i.e., initial disturbances from the shock impinge on the boundary. At that point the boundary conditions produce an in- or outflux of momentum (and the other conserved variables)."
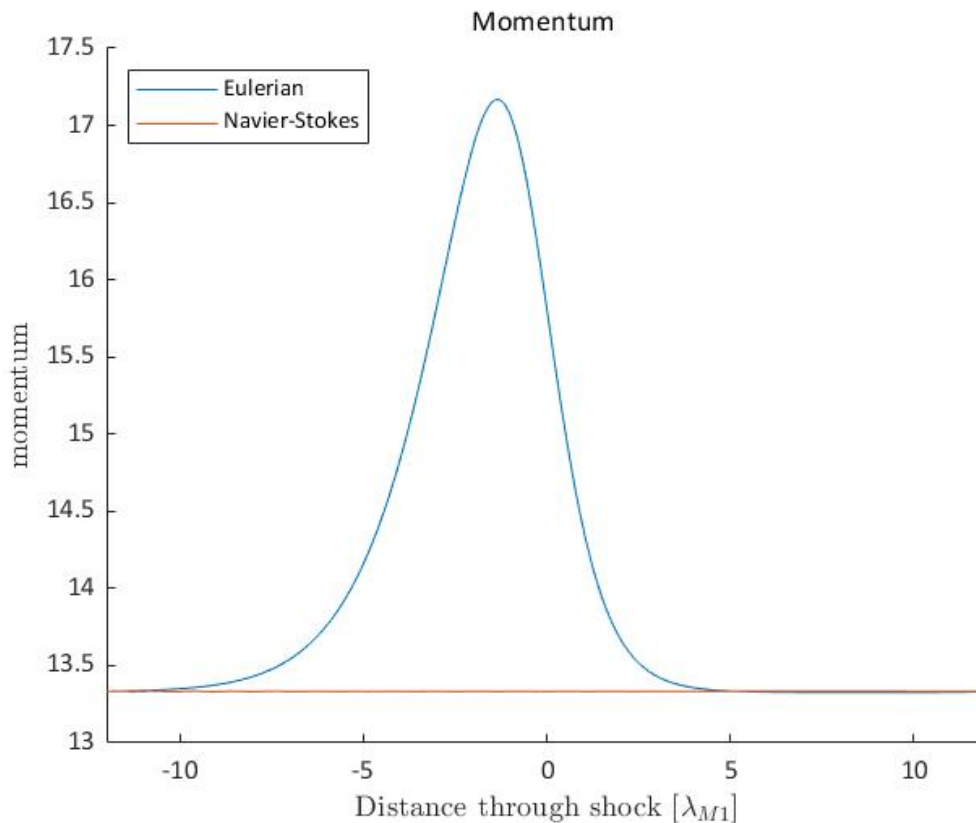

Figure 3.17: Momentum plot for the whole simulated domain $[-12, 12]$, for the best fitting curves. Eulerian model with $\alpha = 4/3$ and constant $\mu = 9.5$. Navier-Stokes with $\mu = \gamma^r T^r$ and $r = 0.76$.

3.4 Overshooting Mach number

Brenner's modification to the Navier-Stokes [Bre05] equation resulted in an overshoot in the Mach number around the discontinuity, see [GR07] for this. It was observed behaviour towards asymptotic overshoot with decreasing cell size, i.e. the higher the number of grid points the larger the overshoot. In [Sva18], it is stated that this phenomenon is non-existing in the new Eulerian model for both $\alpha = 1$ and $\alpha = 4/3$. However, the simulations therein were done with a constant dynamic viscosity and with 100 nodes. Therefore, after seeing the pronounced effect from the power law models, it would be worth the effort to use the same power law as in [GR07] and to increase the number of grid points substantially to see if this still holds.

In the Figure 3.18, three cases are plotted. Two with power law viscosity equivalent to the one used in [GR07], and one with constant dynamic viscosity for comparison. The three curves are all for $\alpha = 4/3$, similar results were obtained with $\alpha = 1$ and not shown for simplicity. The distance between two neighboring grid points, denoted Δx, are $0.024\lambda_1$ and $0.12\lambda_1$ for 1000 and 200 grid points respectively. In [GR07] the overshooting phenomenon is clearly seen at cell sizes of $0.083\lambda_1$ and below.

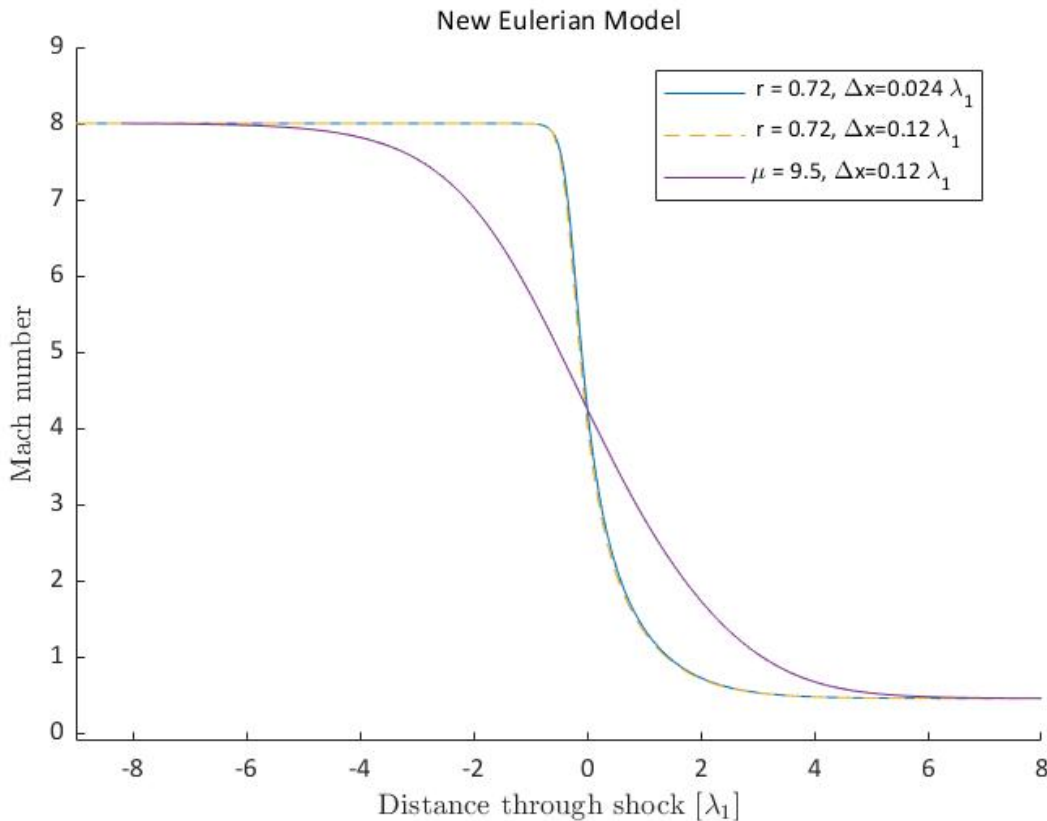Figure 3.18: Mach number plot with power law $\mu = T^r$ for 1000 nodes and 100 nodes. For comparison a curve of constant $\mu = 9.5$ is included.

Obviously there is no overshoot, and the two curves of the power law for 200 nodes and 1000 nodes exactly overlap. There is a sharp drop in the power law curves. This corresponds to the sharp transition for the normalized density plot. Note that, for

a better visual appearance, both curves are shifted so that the mean value of the upstream and downstream Mach number is located at $x = 0$.

No overshoot or unnatural behaviour was observed in the other variables for the Eulerian model.

3.5 Eulerian Alpha Coefficients

For brevity and unnecessary information overload only one figure is presented here although more results have been obtained.

All simulations show that a proper viscosity model and the value of α greatly affect the shock structure. A natural follow up for the power law viscosity would be to increase α to see whether or not one could make the Eulerian model work with this. After all, the anticipated dependency is $\mu \backsim T$. As mentioned in Section 1.6, [Sva18] leaves an opening for the possibility of other values of α than 1 and 4/3.

Below (Figure 3.19), simulated values of $\alpha = \{\frac{4}{3}, \frac{5}{3}, \frac{6}{3}\}$ is shown, with the power law $\mu = T^r$, for $r = 0.72$.
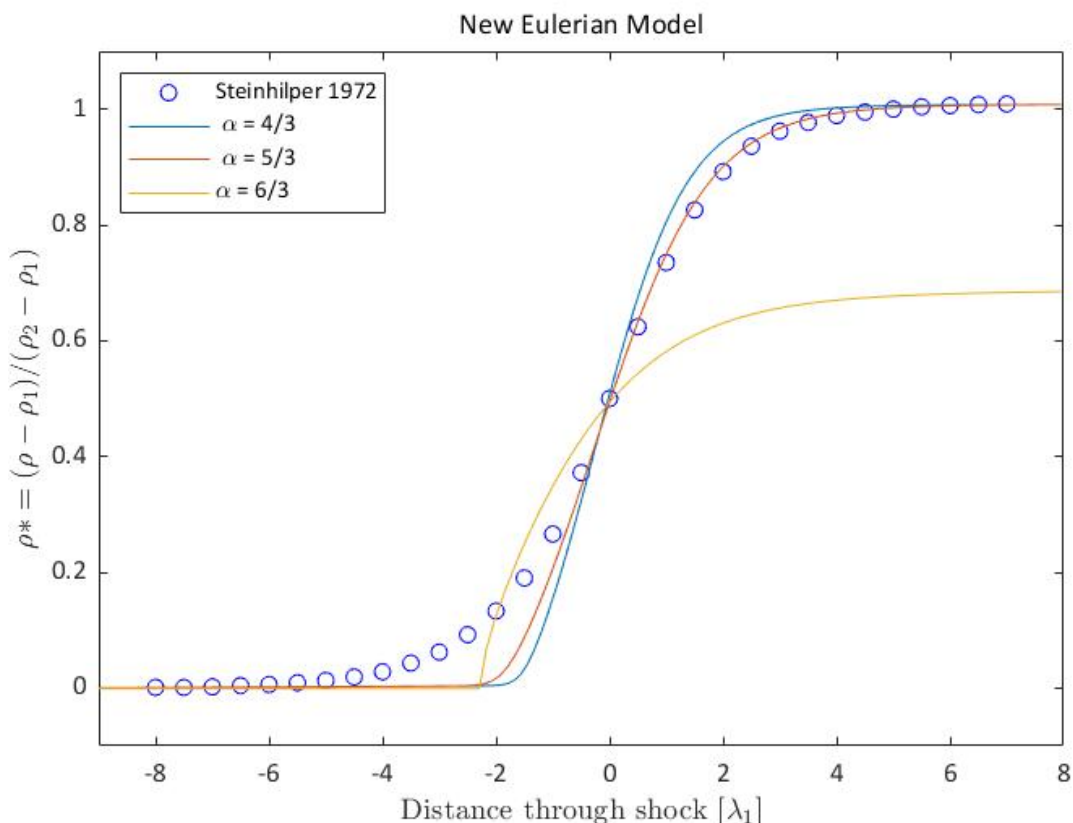
Figure 3.19: Eulerian model with viscosity according to power law $\mu = T^r$ and different values of α

.

The case of $\alpha = 6/3$ fails catastrophically. It reaches the endpoint value, ρ_2, very steeply at the end of the simulated domain $[-12, 12]$ (not shown here.)

For $\alpha = 5/3$ there is a better fit than for $\alpha = 4/3$, but still that sharp transition appears. For higher values of r, the deviation is larger than for $4/3$, and when using $\mu = \gamma^r T^r$, this also catastrophically fails (these results are not shown here).

For constant dynamic viscosity, the effective working of α is merely to stretch/shrink the curve along the x-axis, that is, the same effect as increasing/decreasing μ, respectively. This is also seen from the equations (1.28), since α directly scales μ in $\nu = \alpha \frac{\mu}{\rho}$. Therefore, in the case of constant μ, one can obtain the same results as long as the product $\alpha\mu$, is equal.

Chapter 4

Discussion

4.1 Experimental Uncertainties

Some comments regarding the experimental uncertainties is a good practice to get a better understanding of how close the numerical results are.

The first uncertainty to be mentioned (again) is that the normalized density data in [Ste72] is not exactly equal zero and one at the boundaries. With the small linear scaling (2.32) added, one can only be certain that the endpoints match the experimental data. It is reasonable to *believe* that it also improves the relationship between the experimental and simulated data.

Although the experimental values stem from [Ste72], the experimental uncertainties therein are not explicitly mentioned. Therefore [Als76] is used for this purpose. The experimental setup in [Als76] is a 150 mm diameter shock tube. The density profile is measured by the attenuation of an electron beam, going from an injection needle to a Faraday cage, through a absorption law on the form $\frac{I}{I_0} = A[e^{(-\alpha\rho l)} + B(1 - e^{-\alpha\rho l})$, where I is the electron beam current from injection needle, and I_0 is the beam current measured by the cage. He points out that there are uncertainties due to curvature of shock, velocity measurement among other things. The curvature of the shock is corrected for in [Als76] through a calculation. However, in [Ste72] the diameter of the tube is much larger and it is believed that this curvature due to wall friction effects is negligible. The total uncertainty in the density profile [Als76] is ±4%, but believed to be correct within ±1%. Alsmeyer compares results with Shmidt [Sch69] and for mach numbers between 2.8 - 6.5 the agreement is within ±1%, however, at higher mach number, $M_s = 8$ there is a larger deviation. Alsmeyer, believes these deviations to be from use of an improper absorption law. This fact, points to there being some uncertainties in the way the absorption laws are used to compute the density profile. Therefore one has to allow the mathematical models to not exactly match the experimental values.

Although both system produce good approximations, they are still continuum models applied to a physical problem in the range between a continuum and molecular description.

4.2 Numerical Uncertainties

All simulations have been done with 200, some with 800 and 1000 nodes for comparison. All results were similar.

The validity of using constant dynamic viscosity is clearly debatable, since the general behaviour of a gas is that this increases with temperature. However, the "effective" viscosity used in the Eulerian model is *not* constant owing to its inverse proportionality of the density. The gas in the experiments are also at very low upstream pressures and rarefied and typical Knudsen number is in the range $0.2 < Kn < 0.3$.

When using the upstream values to scale the x-axis as done in Section 2.3.3, the value $\mu_1 = 1$ is set. When using the power law $\mu = \gamma^r T^r$ or constant dynamic viscosity $\mu > 1$, one no longer has that $\mu_1 = 1$. However, as pointed out previously, the viscosity only affects the thickness of the shock. And comparing with the possible range $1 < \mu < 17.8$, as shown in Section 2.3.5, a value of $\mu = 9.5$ is close to a mean value, and therefore not unreasonable.

As stated in Section 2.3.3, the unit length of the scaled x-axis is only approximately equivalent to 1. In fact, it is slightly smaller with 1%. If accounting for this, the numerical values would have been stretch out, giving an even better fit for both the best fitting curves for $x > 0$ (and slightly worse for $x < 0$), since they slightly under-damp compared to the experimental values (since they slightly over-damp compared to the experimental values).

The method used herein have second order accuracy for the interior nodes and first order on the boundary. To capture the shock even better higher order method would be desirable. The SBP-operators used here provide an excellent framework and could be extended to higher order for a comparison. See e.g. [Mat12] for these operators.

4.3 Model Uncertainties

The equation sets (Navier-Stokes and Eulerian) constitutes the ideal gas law. This assumption is well reasoned for in a rarefied gas, in which the spatial occupancy of the molecules are is considered negligible compared to the void. The molecules are thought to only interact with each other through *hard sphere* collisions. However, the higher the pressure and temperature the more faulty this assumption is. In the experiments obtained by Steinhilper, [Ste72], the upstream argon pressure is 25.5 mTorr $\approx$ 0,00003355 atmospheres, i.e. a very low pressure (and probably around room temperature). Similar pressures are also used by Alsmeyer [Als76] (50mTorr) and Schmidt [Sch69] (1mTorr). Hence, the ideal gas law is believed to be of negligible uncertainty.

4.4 Viscosity

As mentioned in Section 1.3 the coefficient of bulk viscosity, $\mu_v = \phi + \frac{2}{3}\mu$, has an appreciable effect on the shock structure. However, viscosity models that include this have not been successfully retrieved from the literature. Articles dealing

with the shock structure problem for reference; [Sva18], [GR07], [Che11], [ESM05] and [RD19], also use the stokes assumption which is consistent with Newtons viscosity law of viscosity for a parallel flow. For a poly-atomic gas, μ_v is generally not zero due to relaxation effects associated with molecular rotation and translation [Kun16]. Rotational effects are not present in a mono-atomic gas which makes stokes assumption more accurate than for a poly-atomic gas. Having a more proper viscosity model with the use of μ_v and still assuming power law form would be in favor for the Navier-Stokes.

4.5 Damping

The complete parabolic nature of the Eulerian model makes it less prone to spurious oscillations. This is clearly an advantage, especially when using central difference operators. For high viscosity the Eulerian model remained stable while Navier-Stokes became more oscillatory, resulting in failure for the case $\mu = \gamma^r T^r$ and $r = 0.81$. This might be overcome by using a more sophisticated boundary procedure.

Chapter 5

Concluding Remarks and Future Work

The main objective in this thesis was to compare the Navier-Stokes equations with the Eulerian model proposed by Svard in [Sva18]. The two system were put into the same framework. The results indicate that for a properly chosen viscosity model (although of debatable validity), both systems are able to approximate a shock in argon gas at Mach 8 within experimental uncertainties.

The coefficient α in the Eulerian model, is suggested to be equal to 4/3 from these results.

The viscosity that suited the Eulerian model best from the simulations done herein was constant $\mu = 9.5$.

For Navier-Stokes the power-law viscosity of the form $\mu = \gamma^r T^r$ and $r = 0.76$ produced the closest approximation to the experimental values.

No overshooting of any variables were observed for the Eulerian model regardless of grid-size h.

The anticipated kinematic viscosity $\nu \backsim \frac{\mu(T)}{\rho(x,t)}$ do not produce as good approximations as $\nu \backsim \frac{\mu}{\rho(x,t)}$, therefore this is suggested to be a more suiting viscosity model for the Eulerian system, in particular for the shock structure problem. Owing to the intermediate Knudsen numbers in this problem, this is not a suggestion of being the more proper model for pure continuum problems.

In summary the Eulerian model perform at least as well as the Navier-Stokes, and it is preferable to numerically work with owing to its more stable and non-oscillatory nature.

For future work:

- A replication of these results are suggested for confirmation. Preferably using higher order methods as well.

- Show stability of this specific problem within the SBP framework.

- Similar analysis for different Mach numbers and compare with experimental values.

- Apply the Eulerian model to "Sod Shock Tube problem" and compare with Navier-Stokes.

- Comparison of constant dynamic viscosity calculations for the Eulerian model, with power law viscosity for Navier-Stokes in pure continuum (low knudsen number) problems.

Bibliography

[Als76]   H. Alsmeyer. Density profiles in argon and nitrogen shock waves measured by the absorption of an electron beam. *Journal of Fluid Mechanics*, 74(3):497–513, April 1976.

[Bre05]   Howard Brenner. Navier–Stokes revisited. *Physica A: Statistical Mechanics and its Applications*, 349(1):60 – 132, 2005.

[Che11]   Pavlo Cherepanov. Shock structure in numerical solutions of the Navier–Stokes and Bhatnagar–Gross–Krook equations. *Mathematical and Computer Modelling*, 53(1):294–309, January 2011.

[ESM05]   Tatiana G. Elizarova, Ivan A. Shirokov, and Salvador Montero. Numerical simulation of shock-wave structure for argon and helium. *Physics of Fluids*, 17(6):068101, 2005.

[Eva10]   L.C. Evans. *Partial Differential Equations*. Graduate studies in mathematics. American Mathematical Society, 2010.

[GR07]   Christopher J. Greenshields and Jason M. Reese. The structure of shock waves as a test of Brenner's modifications to the Navier-Stokes equations. *Journal of Fluid Mechanics*, 580:407–429, June 2007.

[GST01]   Sigal. Gottlieb, Chi-Wang. Shu, and Eitan. Tadmor. Strong stability-preserving high-order time discretization methods. *SIAM Review*, 43:89–112, June 2001.

[Gus08]   Bertil Gustafsson. *High order difference methods for time dependent PDE*. Number 38 in Springer series in computational mathematics. Springer, Berlin, 2008. OCLC: ocn181090541.

[HCB55]   Joseph O. Hirschfelder, C. F. Curtiss, and R. B. Bird. The molecular theory of gases and liquids. *The Journal of the Royal Aeronautical Society*, 59(531):228–228, 1955.

[Kun16]   Cohen Kundu. *Fluid Mechanics, 6Th Edition*. Elsevier India, 6 edition edition, 2016.

[LeV92]   Randall J. LeVeque. *Numerical methods for conservation laws*. Lectures in mathematics ETH Zürich. Birkhäuser Verlag, Basel ; Boston, 2nd ed edition, 1992.

[LT98]   Doron Levy and Eitan Tadmor. From semidiscrete to fully discrete: Stability of runge–kutta schemes by the energy method. *SIAM Review*, 40(1):40–73, 1998.

[Mat03]   Ken Mattsson. Boundary Procedures for Summation-by-Parts Operators. *Journal of Scientific Computing*, 18(1):133–153, February 2003.

[Mat12]   Ken Mattsson. Summation by Parts Operators for Finite Difference Approximations of Second-Derivatives with Variable Coefficients. *Journal of Scientific Computing*, 51(3):650–682, June 2012.

[MSN04] Ken Mattsson, Magnus Svärd, and Jan Nordström. Stable and Accurate Artificial Dissipation. *Journal of Scientific Computing*, 21(1):57–79, August 2004.

[MSS08]   K. Mattsson, M. Svärd, and M. Shoeybi. Stable and accurate schemes for the compressible Navier–Stokes equations. *Journal of Computational Physics*, 227(4):2293–2316, February 2008.

[NC99]   Jan Nordström and Mark H. Carpenter. Boundary and Interface Conditions for High-Order Finite-Difference Methods Applied to the Euler and Navier–Stokes Equations. *Journal of Computational Physics*, 148(2):621 – 645, 1999.

[RD19]   M. H. Lakshminarayana Reddy and S. Kokou Dadzie. Reinterpreting Shock Wave Structure Predictions using the Navier-Stokes Equations. *arXiv:1909.02631 [physics]*, September 2019. arXiv: 1909.02631.

[Sch69]   B. Schmidt. Electron beam density measurements in shock waves in argon. *Journal of Fluid Mechanics*, 39(2):361–373, November 1969. Publisher: Cambridge University Press.

[SCN07]   Magnus Svärd, Mark H. Carpenter, and Jan Nordström. A stable high-order finite difference scheme for the compressible Navier–Stokes equations, far-field boundary conditions. *Journal of Computational Physics*, 225(1):1020–1038, July 2007.

[SN14]   Magnus Svärd and Jan Nordström. Review of summation-by-parts schemes for initial–boundary-value problems. *Journal of Computational Physics*, 268:17–38, July 2014.

[Ste72]   Eric A. Steinhilper. *Electron Beam Measurements of the Shock Wave Structure*. PhD thesis, California Institute of Technology, 1972.

[Sut93]   William Sutherland. Lii. the viscosity of gases and molecular force. *The London, Edinburgh, and Dublin Philosophical Magazine and Journal of Science*, 36(223):507–531, 1893.

[Sva18]   Magnus Svard. A new Eulerian model for viscous and heat conducting compressible flows. *Physica A: Statistical Mechanics and its Applications*, 506:350–375, September 2018.

[TME12] E. Tadmore, R. Miller, and R. Elliot. Continuum Mechanics and Thermodynamics by Ellad B. Tadmor, 2012.

Appendices

Appendix A

SBP Operators

Discrete Operators Second order

Let y_i denote a general discrete variable at node i and h the finite grid length approximating dx.

First derivative operator

$$D_0 y_i = \frac{y_{i+1} - y_{i-1}}{2h} \tag{A.1}$$

yielding the matrix

$$D_0 = \frac{1}{2h} \begin{bmatrix} -2 & 2 & & & & & \\ -1 & 0 & 1 & & & & \\ & -1 & 0 & 1 & & & \\ & & \ddots & \ddots & \ddots & & \\ & & & -1 & 0 & 1 & \\ & & & & -1 & 0 & 1 \\ & & & & & -2 & 2 \end{bmatrix} \tag{A.2}$$

Second derivative operator

$$D_2 y_i = \frac{y_{i+1} - 2y_i + y_{i-1}}{h^2} \tag{A.3}$$

giving the matrix operator

$$D_2 = \frac{1}{h^2} \begin{bmatrix} 1 & -2 & 1 & & & & \\ 1 & -2 & 1 & & & & \\ & 1 & -2 & 1 & & & \\ & & \ddots & \ddots & \ddots & & \\ & & 1 & -2 & 1 & & \\ & & & 1 & -2 & 1 & \\ & & & 1 & -2 & 1 & \end{bmatrix} \tag{A.4}$$

For the variable coefficient matrix denoted $D_2^{(b)}$, and the variable coefficient b, the left boundary closure is given by a 3×3 matrix

$$\begin{bmatrix} \frac{b_1+b_2}{2} & -\left(\frac{b_1+b_2}{2}\right) & 0 \\ -\left(\frac{b_1+b_2}{2}\right) & \frac{b_1+2b_2+b_3}{2} & -\left(\frac{b_2+b_3}{2}\right) \\ 0 & -\left(\frac{b_2+b_3}{2}\right) & \frac{b_2+2b_3+b_4}{2} \end{bmatrix} \tag{A.5}$$

The corresponding right boundary closure is given by replacing $b_i \longrightarrow b_{N+1-i}$ for $i = 1..4$ followed by a permutation of both rows and columns, such that symmetry is obtained.

The interior stencil of $D_2^{(b)}$ at row i is given by $(i = 4...N - 3)$

$$\begin{aligned} m_{i,i-1} &= -\left(\frac{b_{i-1} + b_i}{2}\right) \\ m_{i,i} &= \frac{b_{i-1} + 2b_i + b_{i+1}}{2} \\ m_{i,i+1} &= -\left(\frac{b_i + b_{i+1}}{2}\right) \end{aligned} \tag{A.6}$$

Appendix B

Experimental Data

Table B.1: Experimental data given obtained from Steinhilper [Ste72]. Argon gas at Mach 8, p1=25,50 mTorr, 5 runs.

Experimental Data	
x/λ_1	$\rho^* = \frac{\rho-\rho_1}{\rho_2-\rho_1}$
-8	0,001
-7,5	0,001
-7	0,002
-6,5	0,004
-6	0,006
-5,5	0,009
-5	0,013
-4,5	0,019
-4	0,028
-3,5	0,043
-3	0,062
-2,5	0,092
-2	0,133
-1,5	0,19
-1	0,266
-0,5	0,372
0	0,5
0,5	0,624
1	0,735
1,5	0,826
2	0,892
2,5	0,936
3	0,962
3,5	0,977
4	0,989
4,5	0,995
5	1
5,5	1,004
6	1,006
6,5	1,008
7	1,009